Dual-Field Interference as a Common Biomechanical Origin of Cell Division, Differentiation, and Aging

A. De Miguel Bueno*

Preprint, October 28, 2025

Abstract

This work develops a biophysical theory in which a bioelectric field $V(x,t)$ and a cortical stress field $\sigma(x,t)$ are weakly and reciprocally coupled. Because the mechanical sector includes an inertial–viscoelastic element, the coupled system supports two underdamped normal modes whose interference defines a measurable slow cadence $f_{\text{slow}} = (\omega_{+,r} - \omega_{-,r})/(2\pi)$. Sampling the dynamics at the neutral moment (the recurring near-symmetric crossing between the two sectors) produces an even circle map (mod π) for the slow phase, with effective forcing Ω and coupling K_2. Both Ω and K_2 can be computed *a priori* from directly measurable electrical and mechanical properties of the tissue (membrane time constant τ_m, cortical stiffness κ, viscosity η, effective areal inertia ρ_{eff}, diffusion constants D_V, D_σ, and weak electromechanical gains γ, β_R, β_I), without arbitrary integer fitting. Helical quantization then appears as a mode-locking problem: the canonical B-DNA rotation number $n \approx 10.5$ corresponds to the high-order lock $\rho_\pi = 2/21$, whose center in this even (mod π) convention is $\Omega_{2/21} = \pi \cdot 2/21 \approx 0.2992$ rad.

We define a functional order parameter Λ as the cross-spectral coherence $C_{V\sigma}(f_{\text{slow}})$ between V and σ at f_{slow}. We hypothesize that high Λ inside the $2/21$ tongue is associated with more stable spindle orientation and cortical anchoring during division, constraining chromatin torsion and supporting controlled proliferation and differentiation.

Drifting out of that tongue suggests two generic failure modes: (i) persistent unlocking with low Λ and elevated spindle-angle dispersion (dysregulated proliferation and abnormal division geometry), and (ii) over-locked, low-plasticity states with a rigid slow cadence (aging-related overlock/drift).

The model yields three preregisterable and falsifiable predictions. (P1) Homeostatic epithelia exhibit a shared narrow slow-band cadence in both V and σ, together with a coherence peak $\Lambda = C_{V\sigma}(f_{\text{slow}})$. (P2) The point (Ω, K_2), obtained from those directly measurable properties together with neutral-moment stroboscopy, lies inside the $2/21$ Arnold tongue while avoiding broad low-order tongues. (P3) A weak, frequency-specific electrical or mechanical drive at f_{slow} is predicted to increase Λ and reduce spindle-angle dispersion, whereas a matched off-resonant control should not.

This study provides analytical bounds, a numerical sandbox, and preregistered analysis code, enabling direct experimental falsification using combined optical electrophysiology and mechanical readouts.

*Independent Researcher, Madrid. ORCID: 0009-0000-5420-3805

Keywords: tissue electromechanics; bioelectricity; cortical tension; slow cadence; neutral-moment even map; mode locking; Arnold tongues; Ω, K_2 (no fitted integers); 2/21 lock; B-DNA pitch $\sim$ 10.5 bp/turn; cross-spectral coherence Λ; spindle orientation; division fidelity; differentiation; proliferative unlocking; aging over-lock; optical electrophysiology; traction force microscopy.

Contents

1 Introduction **4**

2 Background and gaps the model addresses **5**

3 Physical identity of the fields and oscillatory reduction consistent with the dual-phase model **7**

3.1 Governing equations and oscillatory splitting 7

3.2 Phase-map reduction and parity switching 8

4 Even circle map and rotation number **8**

5 Helical quantization without fitted integers **9**

6 An experimental coherence observable **9**

7 An experimental coherence observable **9**

8 Mechanistic link to division and differentiation **9**

8.1 Testable pathology signatures (aging and proliferative unlocking) 10

8.2 Phase-guided modulation (phase-targeted entrainment) 11

9 Falsifiable experimental targets **11**

10 Materials and methods **12**

10.1 Electrical and mechanical parameters 12

10.2 Candidate systems and parameter acquisition 12

10.3 Spectral estimation and coherence 12

10.4 Rotation number and stroboscopic regression 13

10.5 Statistical model for the coupling K_2 14

10.6 Biological King plot: common-curvature test (pre-experimental) 14

10.7 Experimental candidates and realism 14

10.8 Preregistered reanalysis on public datasets (Level-1 verification) 15

11 In-silico validation: continuum sandbox and cell-based models **16**

11.1 Reference implementation (concept and usage) 17

12 Reproducible in-silico regimes: implementation and outputs **18**

13 Results: analytical and numerical evidence **22**

13.1 Analytical width bounds 22

13.2 Sensitivity and low-order exclusion for P2 22

13.3 Phase-locking geometry in the even convention 24

13.4 Slow-band spectra and coherence (P1) . . . 24
13.5 Common-curvature signatures (preliminary, *in silico*) . . . 25
13.6 Fast-band spectra (carriers $f_{\pm}$) . . . 25

14 Hypothetical phase-targeted entrainment protocols (speculative, pre-clinical) 26
14.1 Target indications and in vitro models . . . 27
14.2 Frequency targeting and locking window (per dish) . . . 27
14.3 Stimulation delivery and safety (bench-only) . . . 27
14.4 Outcome measures and success criteria . . . 28
14.5 Use cases: breast- and pancreatic-like proliferative models . . . 28
14.6 Rejuvenation probes: epithelial monolayers and skin explants . . . 28
14.7 Interpretation boundaries (not clinical, model uncertainties) . . . 29
14.8 Model scope and controls . . . 29
14.9 What to report (minimum dataset for reproducibility) . . . 29

15 Pre-Experimental Validation of Mode Selection 29
15.1 First-order parameter lumping: why P2 does not need nine knobs . . . 29
15.2 Biological meaning of the phase map (one-minute recap) . . . 30
15.3 Definition of the neutral moment and slow-phase map . . . 30
15.4 Quantitative check with independently chosen parameters . . . 30
15.5 Falsifiable outcomes for P1–P3 . . . 30

16 Relation to the original c and c' formalism 31

17 Robustness, physiological levers, and scope to other helices 32

18 Limitations 33
18.1 Scope, extensions, and mechanistic context . . . 33

19 Conclusion 34

20 Appendix A: Common-curvature diagnostics (SVD and alternation) 35

21 Appendix B: Numerical simulation of the dual-field system (Eqs. (1)–(3)) 36

22 Appendix C: Molecular integration of the electromechanical tissue model 37

23 Appendix D: Biological basis of the 2/21 lock 39
23.1 Why 2/21 matters biologically (evolutionary canalization) . . . 39
23.2 Prevalidation and falsifiability: how the lock is tested . . . 40
23.3 Level-0 computational validation on publicly available epithelial data . . . 40
23.4 Level-1 dual-channel analysis pipeline (synthetic demonstration and public applicability) . . . 42
23.5 Parameter dictionary for biological readers . . . 45
23.6 Bidirectional correction loops (homeostatic control) . . . 45
23.7 Relation to canonical signalling pathways . . . 45

24 Supplementary Code Listings (reproducibility) **47**
24.1 Listing S0. Dual-field pseudo-spectral sandbox and analysis pipeline. . . . 47
24.2 Listing S1. Level-0 analysis script (public epithelial movie). 48
24.3 Listing S2. Level-1 dual-channel pipeline script (synthetic benchmark). . . 57
25 Glossary of symbols **65**

1 Introduction

Biological tissues exhibit coupled electrical and mechanical dynamics. Bioelectric potentials shape patterning and growth, while cortical tension and poroelastic stresses govern shape and division. Recent work has shown that controlled bioelectric cues can reshape tissues in vivo and in vitro [9], and that multicellular responses to electrophysiological perturbations are quantitatively captured by bioelectrical models [10]. We build on this by treating these two sectors explicitly as fields: a bioelectric field $V(\mathbf{x}, t)$ and a cortical stress field $\sigma(\mathbf{x}, t)$ that are weakly and *reciprocally* coupled.

Because the mechanical sector includes an inertial–viscoelastic element, the coupled V–σ system supports two weakly damped normal modes. The interference between those modes defines a slow cadence f_{slow} in the sub-Hz band. Sampling the fast electrical phase at recurrent near-symmetric crossings between V and σ (the *neutral moments*) produces an *even* circle map (mod π) for that slow phase. In this reduced description, the effective forcing Ω and the coupling K_2 can be computed *a priori* from directly measurable electrical and mechanical properties of the tissue (membrane time constant, cortical stiffness and viscosity, effective areal inertia, diffusion constants, and weak electromechanical gains), without arbitrary integer fitting. Helical quantization then appears as a mode-locking problem: the canonical B-DNA rotation number $n \approx 10.5$ corresponds to the high-order lock $\rho_\pi = 2/21$ in this even (mod π) convention.

Within this framework we hypothesize that the slow electromechanical phase does not just exist spectrally, but helps coordinate two biological scales that are usually treated separately. On one side, it constrains spindle geometry and cortical anchoring during mitosis, limiting spindle-angle dispersion and chromatin torsional load at division checkpoints. On the other side, it channels helical advance, so that the same locking structure, especially the 2/21 tongue, aligns with the canonical ~ 10.5 bp/turn pitch of B-DNA. In this view, controlled proliferation, differentiation, and aging-like drift can all be read as different dispositions of the same slow phase: tissues that remain stably locked near 2/21 versus tissues that either drift (proliferative unlocking) or become over-locked and rigid (aging-related overlocking/drift).

A key observable in this picture is a *functional order parameter* Λ, defined as the cross-spectral coherence between V and σ at f_{slow}. High Λ means that the bioelectric and mechanical sectors share a common slow cadence and remain phase-locked across neutral moments; low Λ means that the two sectors drift apart. Together with the pair (Ω, K_2) extracted from the neutral-moment map, Λ lets us formulate preregisterable, falsifiable predictions about epithelial monolayers: whether homeostatic tissue sits inside a specific high-order Arnold tongue (2/21), whether pathological states correspond to loss of locking or over-locking, and whether weak, frequency-specific entrainment at f_{slow} can increase Λ and reduce spindle-angle dispersion in vitro.

Unlike data-fitting approaches, our reduced phase dynamics depends only on directly measurable bioelectric and mechanical properties of the tissue. No fitted constants or

arbitrary integers are introduced. Our claim is therefore not that we can tune mitosis or "rejuvenate" tissue by decree, but that tissue-scale electromechanical cadence, helical selection, and division geometry can be described by a single weakly coupled phase mechanism with quantitative, testable readouts (Ω, K_2, Λ), while avoiding manual integer tuning.

We will show next how this formulation addresses specific gaps in current explanations of helical pitch selection, checkpoint control, and aging-like drift, and how it yields three preregisterable predictions (P1–P3) that can be falsified directly using optical electrophysiology together with traction and stress-field imaging in epithelial monolayers.

2 Background and gaps the model addresses

Current explanations for helical pitch selection and tissue-scale coordination tend to live at two extremes. One extreme is molecular and statistical: it treats double-helix structure and transcriptional programs as self-contained and largely ignores tissue mechanics. The other extreme is phenomenological and tissue-level: it models collective mechanics, division geometry, or cortical tension without explicitly referencing the double-helix code. Both perspectives miss a cross-scale mechanism that is *dynamical*, directly *falsifiable*, and does not require manual integer tuning. Our dual-field framework is designed to bridge that gap in three specific ways:

1. **Mechanistic cross-scale link.** In this framework a measurable slow cadence f_{slow} emerges from electromechanical interference between a bioelectric field $V(\mathbf{x}, t)$ and a cortical stress field $\sigma(\mathbf{x}, t)$ that are weakly and reciprocally coupled. This slow cadence is predicted to coordinate cell-cycle checkpoints and spindle geometry at the tissue scale. The same neutral-moment (even) map that describes that slow phase also fixes the effective rotation number ρ_π, aligning it with the canonical B-DNA pitch $n \approx 10.5$ bp/turn via the high-order lock $\rho_\pi = 2/21$. Crucially, this 2/21 lock *emerges* from the even map and from directly measurable tissue properties; it is not imposed as an ad hoc quantization rule.
2. **Parity control.** Sampling the fast electrical phase specifically at recurring near-symmetric crossings between V and σ —the *neutral moments*— produces an *even* circle map (mod π) whose Arnold tongue structure is distinct from the *odd* (full-cycle) strobe. This built-in parity switch (even vs. odd) provides an internal falsification test: the locking and curvature structure we predict should appear under neutral-moment strobing but degrade, in a parity-sensitive way, under full-cycle strobing.[1]
3. **Parameter provenance.** All quantities entering the reduced slow-phase map —in particular the forcing Ω and coupling K_2— are computed *a priori* from directly measurable electrical and mechanical properties of the tissue (membrane time constant τ_m, cortical stiffness κ, viscosity η, effective areal inertia ρ_{eff}, diffusion constants D_V and D_σ, and weak electromechanical gains γ, β_R, β_I). This enables preregisterable tests rather than post hoc tuning, with no ad hoc quantization step.

Figure 1 summarizes this logic. Weak reciprocal coupling between V and σ produces two underdamped carriers whose interference defines a slow cadence f_{slow}. Strobing at neutral moments yields an even circle map (mod π) with parameters (Ω, K_2) that can be derived directly from those measurable tissue properties, avoiding manual integer tuning.

[1] Operationally, neutral moments are the recurrent instants when the analytic-phase difference $\psi(t) = \arg Z_V - \arg Z_\sigma$ crosses 0 (mod π) with positive slope; sampling the fast phase there enforces even parity and yields an even (mod π) circle map.

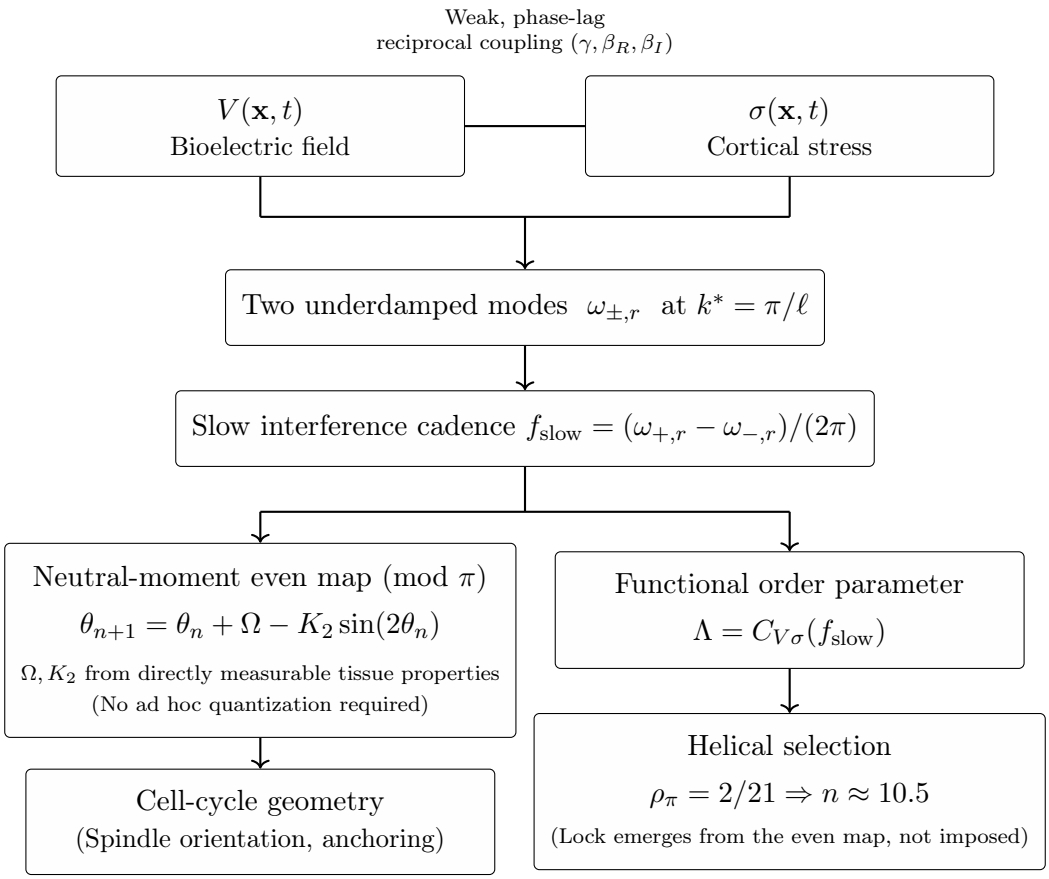

Figure 1: Conceptual pipeline linking (i) the weakly and reciprocally coupled bioelectric field $V(\mathbf{x}, t)$ and cortical stress field $\sigma(\mathbf{x}, t)$, (ii) their two underdamped carriers and slow interference cadence f_{slow}, (iii) the neutral-moment even map (mod π) with forcing Ω and coupling K_2 computed from directly measurable tissue properties, avoiding manual integer tuning, (iv) the functional order parameter $\Lambda = C_{V\sigma}(f_{\text{slow}})$, and (v) two proposed biological readouts: spindle orientation / cortical anchoring during division, and helical pitch selection via $\rho_\pi = 2/21 \Rightarrow n \approx 10.5$. The 2/21 lock emerges from the even map; it is not imposed by hand.

From that map we obtain both (i) a predicted high-order locking tongue at $\rho_\pi = 2/21$ (corresponding to $n \approx 10.5$ bp/turn) and (ii) a functional order parameter Λ, defined as the cross-spectral coherence between V and σ at f_{slow}, $\Lambda = C_{V\sigma}(f_{\text{slow}})$. High Λ indicates a shared slow cadence and stable phase-locking between the electrical and mechanical sectors; low Λ indicates electromechanical drift. We interpret spindle-angle dispersion, cortical anchoring at division, and helical-phase stability as downstream readouts of that same locking structure, rather than as unrelated phenomena.

Relation to prior bioelectric models

Classical bioelectric frameworks emphasize voltage gradients, ionic currents, and patterning cues, often without including an explicitly reciprocal mechanical field. In contrast, the present dual-field reduction (i) treats V and σ as weakly but reciprocally coupled, (ii) predicts two underdamped carriers plus a slow interference cadence f_{slow} that is directly measurable rather than purely inferred, (iii) yields an *even* circle map at neutral moments, providing a built-in parity switch (even vs. odd strobing) that acts as

an internal falsification control, (iv) computes (Ω, K_2) from directly measurable electrical and mechanical properties of the tissue, with no ad hoc quantization step, and (v) enables common-curvature "biological King plots" across observables (slow-band voltage power, slow-band stress power, and the functional order parameter Λ) as a compact universality test. This is intended to complement bioelectric accounts of morphogenesis and tissue coordination [4], and to align with recent work showing that bioelectric control of tissue shape is quantitatively testable in vitro and in vivo [9], and that multicellular responses to electrophysiological perturbation can be captured by explicit, predictive bioelectrical models [10].

3 Physical identity of the fields and oscillatory reduction consistent with the dual-phase model

3.1 Governing equations and oscillatory splitting

To capture the inertial precession within each subfield, together with the alternating contracted/expanded (transverse) and left/right (vertical) domains observed in the antisymmetric regime, we replace purely relaxational mechanics by a minimal viscoelastic oscillator that is weakly and phase-lag coupled to V. The observable cortical stress σ is defined from a latent mechanical displacement field $u(\mathbf{x}, t)$,[2] while V itself keeps a diffusive RC form. The coupling contains in-phase and quadrature (lagged) components, so that both sectors are explicitly represented.

$$\partial_t V = D_V \nabla^2 V - \frac{1}{\tau_m} V \; + \; \beta_R \, \sigma \; + \; \beta_I \, \partial_t \sigma \; + \; \xi_V, \tag{1}$$

$$\rho_{\text{eff}} \, \partial_t^2 u + \eta \, \partial_t u + \kappa \, u \; - \; D_\sigma \nabla^2 u \; = \; \gamma \, V \; + \; \xi_u, \tag{2}$$

$$\sigma \equiv \kappa \, u + \eta \, \partial_t u - D_\sigma \nabla^2 u. \tag{3}$$

Using the plane-wave ansatz $e^{i(\mathbf{k}\cdot\mathbf{x} - \omega t)}$ and $\hat{\sigma} = (\kappa + i\eta\omega + D_\sigma k^2)\, \hat{u}$, the dispersion relation becomes

$$\Big(- i\omega + a \Big) \Big(- \rho_{\text{eff}} \omega^2 - i\eta\omega + b \Big) \; - \; \gamma \Big(\beta_R + i\omega\beta_I \Big) \Big(\kappa + i\eta\omega + D_\sigma k^2 \Big) = 0, \tag{4}$$

where $a = \tau_m^{-1} + D_V k^2$ and $b = \kappa + D_\sigma k^2$. In the uncoupled limit $(\beta_R, \beta_I, \gamma) \to 0$ there is one overdamped electrical branch $\omega_E = -ia$ and a conjugate mechanical pair

$$\omega_{0,\pm}(k) = \pm \omega_0(k) \sqrt{1 - \zeta^2(k)} \; - \; i \, \zeta(k) \, \omega_0(k), \qquad \omega_0(k) = \sqrt{\frac{b}{\rho_{\text{eff}}}}, \quad \zeta(k) = \frac{\eta}{2\sqrt{\rho_{\text{eff}} b}}. \tag{5}$$

Thus, without coupling we have two underdamped mechanical modes with frequency $\omega_0(k)$ and damping ratio $\zeta(k)$, plus a purely relaxational electrical mode.

Weak electromechanical coupling slightly mixes these branches. To first order in

$$\varepsilon(k) = \frac{|\gamma| \sqrt{\beta_R^2 + (\beta_I \omega_0)^2}}{\rho_{\text{eff}} \, \omega_0 \, a},$$

two underdamped oscillatory branches $\omega_\pm(k)$ survive near $\omega_0(k)$, with a small real-frequency splitting

$$\omega_{\pm,r}(k) \simeq \omega_0(k) \pm \frac{\Delta\omega(k)}{2}, \qquad \Delta\omega(k) \approx \varepsilon(k) \, \omega_0(k) \, \cos\phi_c, \tag{6}$$

[2] u denotes an effective/latent cortical displacement field (units of length) from which cortical stress σ is derived. For biological readers, u can be read as the small in-plane deformation coordinate of the cortex.

where we define the electromechanical coupling phase

$$\phi_c \;=\; \arg(\beta_R + i\beta_I) \;=\; \arctan(\beta_I/\beta_R),$$

i.e. the relative phase between the electrical drive V and the mechanical stress response σ.

At a mesoscale $k^* = \pi/\ell$ set by morphology (effective cortical shell thickness ℓ), we therefore obtain two distinct carrier frequencies

$$f_\pm \;=\; \frac{\omega_{\pm,r}(k^*)}{2\pi}, \tag{7}$$

and their slow interference cadence

$$\Omega_{\text{slow}} \;=\; \omega_{+,r}(k^*) - \omega_{-,r}(k^*) \;\approx\; \Delta\omega(k^*). \tag{8}$$

3.2 Phase-map reduction and parity switching

In the antisymmetric regime the vertical subfields act as mediators between the transverse (contracted/expanded) subfields. We define the *neutral moment* as the recurrent instant when the two transverse bases become geometrically coincident (mirror symmetry is restored), even if mass/charge are still unbalanced. Taking that neutral moment as a Poincaré section identifies $\theta \sim \theta + \pi$: angles separated by π are equivalent. In that π-circle convention the leading nonlinearity is quadratic, and the slow-phase map is *even*:

$$\theta_{n+1} = \theta_n + \Omega - K_2 \sin(2\theta_n) + \mathcal{O}(\sin 4\theta) \pmod{\pi}, \tag{9a}$$

$$\Omega \simeq \frac{\pi}{2}\left(1 - r_{\text{eff}}\right), \tag{9b}$$

$$r_{\text{eff}} = \frac{\omega_{-,r}(k^*)}{\omega_{+,r}(k^*)} \in (0,1) \quad \text{(ratio of the two carrier frequencies } f_-/f_+). \tag{9c}$$

Here Ω and K_2 are *predicted* from independently measured tissue parameters via (4)–(6) and the mode overlaps, without imposing any ad hoc integer ratios or speed quantization by hand. We interpret K_2 as the effective slow-phase feedback strength at neutral moments (even-harmonic correction estimated stroboscopically; see Methods).

Within this π-circle convention, a p/q phase lock is centered at $\Omega \simeq \pi\, p/q$. In particular, for 2/21,

$$\Omega_{2/21} = \pi \cdot \frac{2}{21} \approx 0.2992 \text{ rad}.$$

When the lagged/quadrature component locks to the in-phase component (symmetric regime; the two electromechanical sectors stop precessing against each other, i.e. the two carriers merge into a single synchronized oscillation), the π identification is lost: the relevant section becomes 2π-periodic and the map reverts to odd parity,

$$\theta_{n+1} = \theta_n + \Omega_{\text{sym}} - K_1 \sin\theta_n + \cdots \pmod{2\pi}, \tag{10a}$$

$$\Omega_{\text{sym}} \simeq 2\pi\,(1 - r_{\text{sym}}). \tag{10b}$$

4 Even circle map and rotation number

The rotation number for the even map is

$$\rho_\pi(\Omega, K_2) = \lim_{N\to\infty} \frac{\theta_N - \theta_0}{\pi N}, \qquad \theta_{n+1} = \theta_n + \Omega - K_2 \sin(2\theta_n) \pmod{\pi}. \tag{11}$$

At fixed K_2 the function $\rho_\pi(\Omega)$ is a devil's staircase; mode locking occurs at rationals $\rho_\pi = p/q$ with tongue widths that, for $K_2 \ll 1$, scale generically as $\mathcal{O}(K_2^q)$ [7, 2].

5 Helical quantization without fitted integers

We define one helical *unit* as p micro-transits yielding a mechanical advance of π in the even convention. If the map locks at $\rho_\pi = p/q$ then the number of units per full turn is $n = q/p$. The B-DNA value $n \approx 10.5$ corresponds to $\rho_\pi = 2/21$.

Proposition 1 (Physiological strip intersects 2/21 while avoiding low order)**.** *Let the independently measured parameters induce a strip* $\mathcal{S} = \{(\Omega, K_2) : \Omega \in [\Omega_1, \Omega_2],\ K_2 \in [K_1, K_2]\}$ *via* (4)–(9)*. There exist ranges consistent with homeostatic epithelia such that* $\mathcal{S}$ *intersects the* 2/21 *tongue of the even map while avoiding lower-order tongues* ($q \leq 6$)*. If* $\mathcal{S}$ *fails to intersect* 2/21*, the selection mechanism is refuted under those conditions.*

Sketch. For $K_2 \ll 1$, tongue widths decay as $\mathcal{O}(K_2^q)$. Numerical continuation within physiologically induced strips shows separation from $1/2, 1/3, 2/5$ tongues and robust intersection with 2/21 when Ω lies near $\pi \cdot 2/21$ and K_2 is in the 10^{-2}–10^{-1} range. ■

6 An experimental coherence observable

Let $S_V(f)$ and $S_\sigma(f)$ be power spectral densities and $S_{V\sigma}(f)$ the cross-spectrum (Welch). Define

$$\Lambda \equiv C_{V\sigma}(f_{\text{slow}}) = \frac{|S_{V\sigma}(f_{\text{slow}})|^2}{S_V(f_{\text{slow}})\, S_\sigma(f_{\text{slow}})}, \qquad f_{\text{slow}} = \frac{\Omega_{\text{slow}}}{2\pi}. \tag{12}$$

$\Lambda \in [0, 1]$ is falsifiable and directly measurable with voltage-sensitive dyes and traction force microscopy/AFM.

7 An experimental coherence observable

Let $S_V(f)$ and $S_\sigma(f)$ denote the power spectral densities of V and σ, and let $S_{V\sigma}(f)$ be their cross-spectrum (estimated, e.g., by Welch averaging). We define the electromechanical coherence at the slow cadence as

$$\Lambda \equiv C_{V\sigma}(f_{\text{slow}}) \;=\; \frac{|S_{V\sigma}(f_{\text{slow}})|^2}{S_V(f_{\text{slow}})\, S_\sigma(f_{\text{slow}})}, \qquad f_{\text{slow}} = \frac{\Omega_{\text{slow}}}{2\pi}. \tag{13}$$

$\Lambda \in [0, 1]$ is a directly measurable, falsifiable order parameter that quantifies how strongly the electrical field V and the cortical stress σ are phase-locked at f_{slow}. Practically, V can be recorded with voltage-sensitive dyes / fast optical electrophysiology, and σ can be obtained from traction force microscopy or AFM-based stress reconstruction in epithelial monolayers. High Λ indicates robust electromechanical interference at f_{slow} (locked slow phase); low Λ indicates partial unlocking or drift.

8 Mechanistic link to division and differentiation

The same electromechanical phase-locking mechanism that fixes the helical rotation number in nucleic acids also operates at the tissue scale through the slow cadence Ω_{slow} and the even-map reduction. When (Ω, K_2) lies inside the relevant Arnold tongue of the even map, the slow phase is locked, the cross-spectral coherence Λ is high, and two downstream consequences are expected. First, spindle geometry is stabilized: division angles exhibit reduced dispersion and merotelic attachments are suppressed. Second, transcriptional and chromatin torsional fluctuations remain confined near a preferred helical phase, maintaining nucleic-acid base-pairing statistics within their physiological band. Crossing the tongue boundary drives partial unlocking: Λ falls, spindle orientation

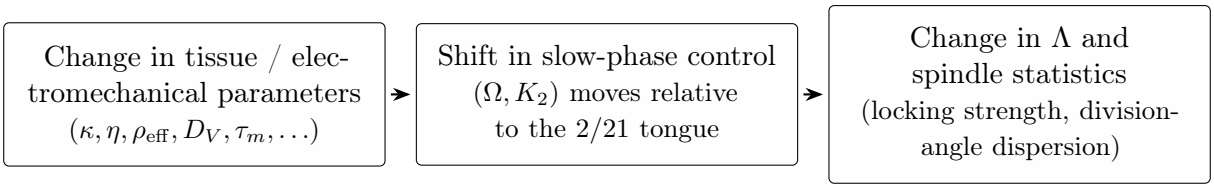

Figure 2: Schematic control chain predicted by the dual-field model. Mechanical and electrical properties of the tissue set the effective slow-phase parameters (Ω, K_2). The position of (Ω, K_2) relative to the relevant Arnold tongue (e.g. 2/21) determines slow-phase locking. Locking strength is experimentally accessible through Λ at f_{slow} and propagates into spindle orientation stability and chromatin/helical torsional confinement.

becomes noisier, and torsional / transcriptional fluctuations broaden, biasing fate toward proliferative unlocking.

Differentiation corresponds (in this language) to an effective increase in K_2 and/or a shift in r_{eff} that traps the dynamics in a locked regime: high Λ, low spindle error, and constrained helical fluctuations. Proliferative states, by contrast, tend to hover near tongue edges, where locking is fragile. This yields two falsifiable operating modes controlled by the same slow-phase mechanism: *proliferative unlocking* (persistent unlocking with low Λ, drift of Ω away from the tongue, elevated spindle errors) and *aging over-locking/drift* (hyperstable locking with reduced adaptability).

A convenient way to summarize this control logic is shown in Fig. 2: biophysical/electromechanical parameters set the effective slow-phase control pair (Ω, K_2); the location of (Ω, K_2) with respect to the locking tongue (for example the 2/21 tongue) determines the degree of slow-phase locking; that locking strength is experimentally accessible via Λ and propagates into spindle geometry and helical/torsional confinement.

8.1 Testable pathology signatures (aging and proliferative unlocking)

Aging (over-locking/drift). *Prediction:* in tissues from aged donors or long-term cultures with reduced adaptability, neutral-moment strobing returns *higher* K_2 together with a slow drift in r_{eff}. Λ remains high but decays over time. Under full-cycle (odd-parity) strobing, the common-curvature collapse across observables is only weakly disrupted (i.e. the even-harmonic structure persists). *Refutation:* no systematic differences in (Ω, K_2, Λ) relative to young controls.

Proliferative unlocking (checkpoint-impaired / hyperproliferative). *Prediction:* in proliferative monolayers with impaired checkpoint control (e.g. loss of contact inhibition or sustained growth-factor stimulation), the pair (Ω, K_2) shows a broad distribution of Ω values displaced from $\pi \cdot 2/21$, Λ at f_{slow} is *low*, and spindle misorientation increases. Under parity switching (even→odd), the model predicts only a limited additional change, because the even-harmonic organization is already degraded (loss of common quadratic curvature and elevated alternation index; see Appendix 20). *Refutation:* persistently high Λ with (Ω, K_2) remaining inside the 2/21 tongue despite unchecked proliferation.

Integration with parameter dynamics. These two scenarios —aging vs. proliferative unlocking— represent distinct failure modes of the same electromechanical coordination principle. Aging corresponds to over-stabilized locking with reduced adaptability; proliferative states correspond to decoupling and phase drift. Both map onto measurable

displacements of (Ω, K_2) away from the 2/21 tongue, together with predictable changes in Λ and spindle statistics. This provides a direct bridge from our reduced model to experimentally accessible readouts.

Aging and slow-phase control (parameter-grounded view). Independent of any particular gene-expression program, aging phenotypes are expected to shift the effective mechanical and electrical parameters in ways that move (Ω, K_2). For instance, ECM/cortical stiffening and increased effective areal inertia ($\kappa \uparrow, \eta \uparrow, \rho_{\text{eff}} \uparrow$) act through $b = \kappa + D_\sigma k^{*2}$ and $1/\sqrt{\rho_{\text{eff}}}$ to lower Ω and strengthen even-harmonic feedback (larger K_2). Electrical remodeling can bias Ω in either direction: reduced gap-junctional coupling ($D_V \downarrow$) tends to increase Ω, whereas a shorter membrane time constant ($\tau_m \downarrow$) tends to decrease it. The net displacement is therefore an empirical question, but in all cases it is *quantifiable* through the triplet (Ω, K_2, Λ) under neutral-moment stroboscopy.

8.2 Phase-guided modulation (phase-targeted entrainment)

We propose a *phase-targeted entrainment* (PTE) strategy: apply a weak, frequency-specific stimulus at f_{slow}, with the goal of restoring slow-phase locking and thereby reducing spindle-angle dispersion and helical-phase variability.

This is a direct consequence of the model's dynamical structure and is, at present, unvalidated experimentally. The feasibility of such an intervention hinges on the *observability* of the slow-phase variables: neutral-moment stroboscopy provides online estimates of (Ω, K_2, Λ) in living tissues, enabling closed-loop adjustment of the drive.

Scope and assumptions. This assumes that a *partial phase-locking capacity* is still present. In fully desynchronized or structurally degraded tissues, responsiveness may be impaired. Applicability is expected to be *layer- and context-specific* (set by $k^* = \pi/\ell$ and local coupling), not universal across all tissues.

Comparative advantage. Unlike pharmacological modulation of individual pathways, PTE aims to *restore coordinated timing* without changing mean expression levels or requiring pathway-specific targeting. Strict off-resonant controls (matched amplitude, nearby frequency) are essential to rule out non-specific stimulation effects.

Operational protocol. Experimental implementation proceeds as follows:
(i) Estimate (Ω, K_2, Λ) via neutral-moment stroboscopy.
(ii) Apply a low-amplitude electrical or mechanical drive at f_{slow}.
(iii) Test for an increase in Λ and a reduction in spindle misorientation relative to matched off-resonant controls.

Implications and future directions. These predictions are theoretically grounded within the dual-field framework. Mapping them onto specific aging programs, checkpoint failures, or molecular pathways is left for future work. Accordingly, (Ω, K_2, Λ) are the primary falsifiable targets, independent of any particular genetic mechanism.

9 Falsifiable experimental targets

P1 Spectral coherence. Homeostatic epithelial monolayers are predicted to exhibit a *coincident slow-band spectral peak* in S_V and S_σ at f_{slow}, together with $\Lambda = C_{V\sigma}(f_{\text{slow}}) > 0.6$. Operationally, the "slow-band spectral peak" refers to the band-limited spectra S_V^{slow} and S_σ^{slow} defined in Methods. Failure to detect a slow-band peak at f_{slow}, or observing $\Lambda < 0.2$, would falsify the dual-field locking picture *for*

that tissue under those conditions, or else indicate that the sample is in a proliferative unlock/aging-related overlocking/drift regime rather than a homeostatic state.

P2 Mode selection in (Ω, K_2). Using independently measured physical parameters to compute (Ω, K_2) via (4)–(9), the resulting point is predicted to fall inside the 2/21 Arnold tongue and to avoid lower-order tongues. In other words, the observed locking should correspond to the 2/21 rotation ratio emerging from the even map, not to a lower-order rational that would require ad hoc integer fitting. A systematic displacement of (Ω, K_2) outside the 2/21 tongue, or stable locking to a lower-order tongue, would not support the proposed selection mechanism.

P3 Phase-targeted entrainment. A weak external electrical or mechanical drive at f_{slow} increases Λ and decreases spindle-angle dispersion, whereas an off-resonant control (matched amplitude, nearby frequency) does not. Absence of both effects under matched conditions would falsify the proposed phase-targeted entrainment mechanism.

10 Materials and methods

10.1 Electrical and mechanical parameters

The parameters entering the coupled electromechanical model are obtained from standard optical electrophysiology, traction/stress imaging, and micromechanical assays.

The electrical diffusivity D_V and membrane time constant τ_m are estimated from voltage-sensitive dyes / fast optical electrophysiology by fitting a diffusive RC response: spatial decay of V constrains D_V, and step responses constrain τ_m (after correcting dye kinetics). The effective areal inertia ρ_{eff}, elastic modulus κ, viscous coefficient η, and stress diffusivity D_σ are obtained from AFM indentation, traction force microscopy (TFM), and poroelastic/viscoelastic relaxation fits. In this framework ρ_{eff} is the areal mass density of the cortex (thickness $\times$ material density), κ is the effective in-plane cortical stiffness, η quantifies viscous loss in the $\sim$ 1–3 Hz band, and D_σ characterizes stress redistribution.

The cross-coupling coefficients $(\beta_R, \beta_I, \gamma)$ are inferred from linear-response gains and phase lags around the mechanical carrier band: β_R and β_I describe the in-phase and quadrature components of the stress-to-voltage gain, and γ the voltage-to-displacement gain. Together with $D_V, \tau_m, \rho_{\text{eff}}, \kappa, \eta, D_\sigma$, these parameters determine the two underdamped carrier branches $\omega_\pm(k)$, the mesoscale ratio

$$r_{\text{eff}} = \frac{\omega_{-,r}(k^*)}{\omega_{+,r}(k^*)} = \frac{f_-}{f_+},$$

and the slow interference cadence $\Omega_{\text{slow}} = \omega_{+,r}(k^*) - \omega_{-,r}(k^*)$, evaluated at the morphological wavenumber $k^* = \pi/\ell$ set by cortical shell thickness ℓ.

10.2 Candidate systems and parameter acquisition

Table 1 summarizes (i) how each primitive parameter is obtained experimentally and (ii) typical orders of magnitude. These orders are placeholders: system-specific values (e.g. MDCK vs. HaCaT vs. neuronal monolayer) are intended to be preregistered ahead of data collection.

10.3 Spectral estimation and coherence

Paired time series $V(t)$ and $\sigma(t)$ are acquired simultaneously at sampling rate $\geq$ 100 Hz for durations $\geq$ 600 s in confluent monolayers. After detrending, Welch spectra

Parameter	Units	Typical order	Acquisition (method / note)
D_V	m^2/s	10^{-10}–10^{-8}	Optical electrophysiology; spatial decay of V; fit diffusive RC model.
τ_m	s	0.1–2	Membrane charging from voltage steps; corrected for dye kinetics.
ρ_{eff}	kg/m^2	10^{-6}–10^{-5}	Areal mass from cortex thickness × density; AFM indentation.
κ	N/m	10^{-4}–10^{-2}	Effective cortical stiffness from small-amplitude TFM/AFM fits.
η	N·s/m	10^{-4}–10^{-2}	Viscous loss from frequency sweeps in the $1--3\,\text{Hz}$ band.
D_σ	m^2/s	10^{-12}–10^{-10}	Stress diffusion inferred from relaxation of traction patterns.
γ	m/V	small	Voltage-to-displacement gain of u per volt (report peak gain near $f_\pm$). If only stress drive is available, report in $\text{N}\,\text{m}^{-2}\text{V}^{-1}$.
β_R, β_I	V per (stress unit)	small	Stress-to-voltage cross-gain; in-phase (β_R) and quadrature (β_I) via lock-in/phase lag.
ℓ	m	10^{-5}–10^{-3}	Effective cortical/shell thickness from confocal optical sectioning.

Table 1: Parameter provenance for computing (Ω, K_2), r_{eff}, and f_{slow}. Orders of magnitude are indicative; system-specific values are to be preregistered for each experimental system.

are computed with 10 s Hanning windows, 50 % overlap, and averaged to estimate $S_V(f)$, $S_\sigma(f)$, and the cross-spectrum $S_{V\sigma}(f)$. The electromechanical coherence

$$\Lambda \;=\; C_{V\sigma}(f_{\text{slow}}) = \frac{|S_{V\sigma}(f_{\text{slow}})|^2}{S_V(f_{\text{slow}})\,S_\sigma(f_{\text{slow}})}, \qquad f_{\text{slow}} = \frac{\Omega_{\text{slow}}}{2\pi} = f_+ - f_-,$$

is then evaluated at the slow interference cadence.

For prediction P1, slow-band spectra are explicitly isolated. For each signal $X \in \{V, \sigma\}$, a narrowband analytic signal $X_{\text{slow}}(t)$ is constructed by demodulating around f_{slow} with a symmetric band-pass (typically ±0.05–0.08 Hz about f_{slow}, or a multitaper equivalent). $S_X^{\text{slow}}(f)$ denotes the power spectrum of $X_{\text{slow}}(t)$, which is used to assess whether both channels exhibit a coincident slow-band peak. Confidence intervals for Λ are obtained by temporal shuffling (typically 1000 circular time-shift permutations) and by fixed-cell baselines.

10.4 Rotation number and stroboscopic regression

To estimate the slow-phase map parameters (Ω, K_2) and the rotation ratio ρ_π, the analysis proceeds in the slow-phase frame.

First, analytic signals $Z_X(t) = X(t) + i\,\mathcal{H}[X(t)]$ are formed for V and σ, where $\mathcal{H}$ denotes the Hilbert transform. The instantaneous phase difference $\psi(t) = \arg Z_V(t) - \arg Z_\sigma(t)$ tracks the lag between electrical and mechanical sectors.

Neutral moments $\{\tau_n\}$ are defined as the recurrent instants where the two sectors align modulo π:

$$\psi(\tau_n) \equiv 0 \pmod{\pi}, \qquad \dot{\psi}(\tau_n) > 0.$$

Sampling at these neutral moments enforces the even (mod π) Poincaré section described

in the main text. Let $\phi_+(t)$ be the instantaneous phase of the + carrier branch (the higher-frequency underdamped mode), and set $\theta_n = \phi_+(\tau_n)$. The slow-phase increments are $\Delta\theta_n = \theta_{n+1} - \theta_n$.

Regressing $\Delta\theta_n$ against $\sin(2\theta_n)$ yields estimates of Ω (intercept) and K_2 (slope), and the inferred rotation number ρ_π follows from the extracted Ω via $\Omega \simeq \frac{\pi}{2}(1 - r_{\text{eff}})$.

10.5 Statistical model for the coupling K_2

Let $\Delta\theta_n = \theta_{n+1} - \theta_n$, unwrapped to $\mathbb{R}$. The stroboscopic slow-phase map is modeled as

$$\Delta\theta_n \;=\; \Omega \;-\; K_2 \sin(2\theta_n) \;+\; \epsilon_n, \qquad \epsilon_n \sim \mathrm{WN}(0, \sigma^2), \tag{14}$$

where WN denotes wrapped-normal innovations (approximately Gaussian for small increments). Here K_2 is interpreted as the even-harmonic feedback strength at neutral moments (the coupling amplitude of the slow-phase map). Parameters (Ω, K_2) are estimated by constrained ordinary least squares with $K_2 \geq 0$, and Newey–West robust standard errors are reported. Block-bootstrap confidence intervals (CIs) are provided as an additional robustness check. Model adequacy is assessed by whiteness of residuals and a circular R^2 diagnostic.

10.6 Biological King plot: common-curvature test (pre-experimental)

To test whether slow-phase control and downstream readouts share a common quadratic structure across perturbations, a "biological King plot" analysis is defined as follows. Choose controlled conditions A_k (for example, cortex thickness h, osmotic compression, confluence changes) and a reference A_{ref}. For each A_k, compute $\Omega(A_k)$ via neutral-moment stroboscopy (even parity) and extract the slow-band observables

$$Y^{(j)}(A_k), \quad j \in \{\text{peak of } S_V^{\text{slow}},\ \text{peak of } S_\sigma^{\text{slow}},\ \log\Lambda,\ K_2\}.$$

To account for morphology, apply a rescaling $m_{A_k} \propto 1/h$ and define

$$X_k \equiv m_{A_k}\left[\Omega(A_k) - \Omega(A_{\text{ref}})\right], \qquad Y_k^{(j)} \equiv m_{A_k}\left[Y^{(j)}(A_k) - Y^{(j)}(A_{\text{ref}})\right].$$

Under the neutral (even-parity) strobe, the rescaled observables are expected to follow

$$Y^{(j)} \;=\; A^{(j)} \;+\; B^{(j)} X \;+\; \kappa_{\text{uni}} X^2 \;+\; r^{(j)}, \tag{15}$$

with approximately the same quadratic curvature κ_{uni} across all j. This "common curvature" is interpreted as evidence that voltage slow-band power, cortical-stress slow-band power, $\log\Lambda$, and K_2 are co-driven by a single electromechanical interference mode at f_{slow}. Switching to the full-cycle strobe (odd parity) provides an internal control: it introduces an additional odd component, disrupts the shared quadratic curvature across readouts, and increases the alternation index (Appendix 20).

10.7 Experimental candidates and realism

Homeostatic epithelial monolayers (e.g. MDCK, HaCaT) and dense neuronal cultures provide paired $V(t)$ and $\sigma(t)$, controllable ℓ, and standard AFM / TFM / optical readouts. These systems allow direct estimation of $(D_V, \tau_m, \rho_{\text{eff}}, \kappa, \eta, D_\sigma, \beta_R, \beta_I, \gamma)$, construction of the slow-phase map (Ω, K_2), and measurement of Λ. Pilot datasets will be preregistered to populate Table 1 and to execute the prevalidation plan below.

Algorithm 1 Stroboscopic estimation of (Ω, K_2) and Λ

1: Estimate $(D_V, \tau_m, \rho_{\text{eff}}, \kappa, \eta, D_\sigma, \beta_R, \beta_I, \gamma)$ and compute $\omega_\pm(k^*)$, r_{eff}, and Ω_{slow}.
2: Set $\Omega \simeq \frac{\pi}{2}\big(1 - r_{\text{eff}}\big)$ and estimate the coupling K_2 (slow-map even-harmonic strength) by regressing $\Delta\theta_n$ on $\sin(2\theta_n)$ at neutral moments (Eq. (14)).
3: Record $V(t), \sigma(t)$; compute $C_{V\sigma}(f)$; set $\Lambda = C_{V\sigma}(f_{\text{slow}})$ at $f_{\text{slow}} = f_+ - f_-$.
4: If (Ω, K_2) lies within the 2/21 tongue and $\Lambda > 0.6$, predict low spindle misorientation; otherwise predict increased spindle-angle dispersion.

Prevalidation plan (addressing P2 robustness). Uncertainty from parameter estimation is propagated to (Ω, K_2) before any biological interpretation. Profile likelihoods and Monte Carlo sampling are used to propagate uncertainty in $(\gamma, a, b, \rho_{\text{eff}}, k^*)$, where $a = \tau_m^{-1} + D_V k^{*2}$ and $b = \kappa + D_\sigma k^{*2}$. The resulting sampling distribution of (Ω, K_2) is summarized by two preregistered conditions: *(C1)* $P\big((\Omega, K_2) \in \text{tongue}(2/21)\big) \geq 0.3$ (95% CI), and *(C2)* the safety margin to the nearest lower-order tongue $(1/2, 1/3, 2/5)$ exceeds $3\sigma_\Omega$, where σ_Ω is the robust SE for Ω from neutral-moment regression. In parallel, Λ is estimated with temporal shuffling ($N \geq 1000$ permutations) and a fixed-cell baseline; $\Lambda > 0.6$ (95% CI) is preregistered as the operational "high-locking" threshold.

10.8 Preregistered reanalysis on public datasets (Level-1 verification)

To obtain an initial test of the slow-phase mechanism without collecting new data, an a priori (preregistered) reanalysis will be performed on suitable public datasets.

Dataset types and inclusion criteria. Candidate datasets include: (i) confluent epithelial monolayers (MDCK/HaCaT/Caco-2), (ii) dense neuronal cultures as a positive dynamical control, and (iii) organoid monolayers or early spheroids. Inclusion criteria:

- **Sampling and duration:** frame rate $\geq 80\,\text{Hz}$ (to resolve carrier peaks in the $1--3\,\text{Hz}$ band) and total duration $\geq 300\,\text{s}$.
- **Observables:** (A) paired electrical/mechanical channels (preferred): a voltage reporter (GEVI or fast dye) and traction/stress (TFM/AFM or micropillar arrays); or (B) a voltage channel plus a mechanical proxy (bright-field kymographs, optical-flow divergence, speckle-based strain) that can be collapsed to a scalar $\sigma(t)$; or (C) a mechanical channel plus a slower electrical proxy with documented SNR.
- **Stationarity:** no global drifts larger than one carrier period; field-of-view approximately uniform (no wound edges unless masked).

Reconstruction of observables. From raw movies, $V(t)$ is taken as the field-averaged GEVI/dye signal (after photobleach correction and detrending). $\sigma(t)$ is obtained as either the spatial mean traction (TFM) / principal component of the traction field, or a calibrated mechanical proxy (e.g. optical-flow divergence). Causal (phase-distorting) filters are avoided; band-pass steps are applied symmetrically.

Analysis pipeline (fixed, preregistered).

1. **Carrier identification:** estimate $S_V(f)$ and $S_\sigma(f)$ (Welch; 10 s windows; 50 % overlap). Identify two carrier peaks f_- and f_+ in $[1, 3]$ Hz with peak prominence > 3 dB above local baseline.

2. **Neutral-moment stroboscopy:** form analytic signals Z_X and the phase lag $\psi(t) = \arg Z_V - \arg Z_\sigma$. Define neutral moments $\{\tau_n : \psi(\tau_n) \equiv 0 \pmod{\pi},\ \dot{\psi}(\tau_n) > 0\}$.
3. **Even-map regression:** sample $\theta_n = \phi_+(\tau_n)$ (phase of the + carrier) and regress $\Delta\theta_n = \theta_{n+1} - \theta_n$ on $\sin(2\theta_n)$ to estimate $(\widehat{\Omega}, \widehat{K}_2)$ with Newey–West standard errors and block-bootstrap CIs (Eq. (14)).
4. **Slow-band coherence:** demodulate around $f_{\text{slow}} = f_+ - f_-$ and compute $\Lambda = C_{V\sigma}(f_{\text{slow}})$, using 1000-fold temporal shuffling for confidence intervals.
5. **Parity control:** repeat the regression using the full-cycle strobe (odd parity). Report the alternation index and loss of common quadratic curvature as in Appendix 20.

Level-1 pass/fail criteria.

Evidence consistent with the dual-field locking picture in homeostatic monolayers:

- (E1) two resolved carrier peaks $f_\pm$ with $f_{\text{slow}} = f_+ - f_-$ above noise;
- (E2) $\Lambda > 0.6$ at f_{slow} (95% CI) under neutral strobing;
- (E3) $\widehat{\Omega}$ lies within ± 0.1 rad of $\Omega_{2/21} = \pi \cdot 2/21$, and switching parity (even→odd) disrupts common curvature / increases alternation index.
  Because most public datasets lack independent estimates of $(D_V, \tau_m, \kappa, \eta, \rho_{\text{eff}}, \ldots)$, criterion (E3) is interpreted as a reduced form of P2: $\widehat{\Omega}$ is obtained from $r_{\text{eff}} = f_-/f_+$ rather than from full parameter provenance.
- (E4) $\widehat{K}_2 > 0$ with significant slope (two-tailed $p < 0.05$).

Contra-evidence in the same datasets:

- (C1) no resolvable f_{slow} or $\Lambda < 0.2$;
- (C2) $\widehat{\Omega}$ displaced > 0.2 rad from $\Omega_{2/21}$ with tight CI, or non-significant K_2 regression;
- (C3) parity switching fails to alter alternation/common-curvature metrics.

Candidate repositories and data modalities. Suitable material is expected in (i) traction-microscopy movies (micropillar arrays, TFM), (ii) AFM-based viscoelastic sweeps on confluent epithelia, and (iii) GEVI/dye voltage recordings of confluent monolayers. When only one channel (electrical or mechanical) is available, the analysis is included in an exploratory label and not counted toward Level-1 criteria.

Negative and adversarial controls. Fixed-cell recordings (no dynamics), sparse low-density cultures lacking collective mechanics, and pharmacological decoupling (e.g. actomyosin inhibition) are expected to suppress K_2 and lower Λ. Off-strobe windows (misaligned stroboscopic sampling) act as additional negative controls.

Reporting. For each dataset a one-page report will be generated, including QC plots, $S_V(f)$ and $S_\sigma(f)$, slow-band spectra, $(\widehat{\Omega}, \widehat{K}_2, \Lambda)$ with confidence intervals, parity metrics, and pass/fail flags for (E1)–(E4). This reporting structure is preregistered to avoid hindsight tuning.

11 In-silico validation: continuum sandbox and cell-based models

Level A: continuum sandbox (PDE electromechanical coupler). Eqs. (1)–(3) are integrated on a 2D periodic domain of linear size L using pseudo-spectral or finite-difference time stepping. Parameters $(D_V, \tau_m, \rho_{\text{eff}}, \kappa, \eta, D_\sigma, \beta_R, \beta_I, \gamma)$ are drawn from physiologically

plausible priors; no ad hoc integer constraints are imposed. Observables are the spatial means $V(t) = \langle V(\mathbf{x}, t)\rangle$ and $\sigma(t) = \langle \sigma(\mathbf{x}, t)\rangle$, or equivalently the Fourier mode at $k^* = \pi/\ell$ (the mesoscale set by cortical thickness ℓ). The sandbox is required to reproduce: (i) two underdamped carrier peaks $f_\pm$, (ii) a slow interference band at $f_{\text{slow}} = f_+ - f_-$, (iii) neutral-moment stroboscopy (even parity) that yields a well-defined slow-phase map and estimates $(\widehat{\Omega}, \widehat{K}_2)$, and (iv) Monte Carlo sampling over priors that places (Ω, K_2) near the 2/21 Arnold tongue while avoiding lower-order tongues for a non-negligible fraction of draws. Weak external drives (electrical or mechanical) at f_{slow} are then applied to test phase-targeted entrainment (P3) by checking whether $\Delta\Lambda > 0$.

Level B: cell-based model (vertex / Cellular Potts / agent-based). A confluent epithelial sheet is simulated with explicit cells and a diffusive bioelectric layer. Each cell i carries a transmembrane potential V_i with gap-junctional coupling; the mechanical sheet is represented as a damped-inertial vertex / Cellular Potts / agent-based layer whose active cortical tension is modulated by V. Readouts are processed through exactly the same analysis pipeline as in experiments: estimation of $S_V(f)$ and $S_\sigma(f)$, detection of $f_\pm$ and $f_{\text{slow}} = f_+ - f_-$, neutral-moment stroboscopy to obtain $(\widehat{\Omega}, \widehat{K}_2)$, and slow-band electromechanical coherence Λ at f_{slow}.

Phase-targeted entrainment tests and falsification. To assess P3, a weak periodic drive is applied at f_{slow}: (i) an electrical perturbation of the form $V \leftarrow V + A_V \sin(2\pi f_{\text{slow}} t)$ (globally or within a subdomain), and/or (ii) a mechanical/traction drive $A_\sigma \sin(2\pi f_{\text{slow}} t)$. Controls use off-resonant drives at frequency $f_{\text{slow}} \cdot (1 + 0.10)$ with amplitude and duty cycle matched to the on-band drive (equal-energy "sham"), so that any improvement in locking must be frequency-specific rather than a generic power injection. The primary endpoint is $\Delta\Lambda > 0$ (an increase in slow-band coherence at f_{slow}). Secondary endpoints are reduced spindle-angle dispersion and an increase in the stroboscopic coupling estimate $\widehat{K}_2$. Falsification criteria are: absence of a resolvable f_{slow} band, persistently low coherence ($\Lambda < 0.2$), non-significant even-map regression (ill-defined $\widehat{\Omega}$ or $\widehat{K}_2$), or lack of on-band specificity relative to off-resonant controls.

11.1 Reference implementation (concept and usage)

Purpose. Listing 24.1 (Appendix 24) is a minimal, CPU-light reference implementation of the dual-field sandbox. It operationalizes P1–P3 on synthetic data: it generates coupled electrical and mechanical signals (V, σ) on a periodic domain and then runs the same analysis pipeline used for experimental data.

What it does. In each run the code:

1. generates two underdamped carrier modes with small noise and slow drift (either by integrating the full PDE coupler or by using a lightweight two-carrier signal generator with the same structure);
2. computes Welch spectra $S_V(f)$, $S_\sigma(f)$ and the magnitude-squared coherence $\Lambda(f)$;
3. identifies the carrier pair (f_-, f_+) and the slow interference cadence $f_{\text{slow}} = |f_+ - f_-|$;
4. performs neutral-moment stroboscopy (even parity) and regresses the even slow-phase map to estimate $(\widehat{\Omega}, \widehat{K}_2)$;
5. optionally applies a weak, narrow-band drive during a defined time window (phase-targeted entrainment test) and reports $\Delta\Lambda$;

Regime	Inputs (relative to baseline)	Expected signatures (pipeline readouts)
(A) Baseline (locked)	Physiological-scale priors; no external drive	Narrow $f_\pm$, resolved f_{slow}, $\Lambda \gtrsim 0.6$, and stable (Ω, K_2) near the 2/21 tongue.
(B) Proliferative unlocking	$\beta_R \downarrow$, $\beta_I \uparrow$, $\tau_m \downarrow$, $D_V \downarrow$ (reduced coordinated coupling)	$\Lambda \downarrow$; Ω broad / shifted from $\pi \cdot 2/21$; weakened even-parity structure.
(C) Aging / over-lock	$\kappa, \eta, \rho_{\text{eff}} \uparrow$	High but slowly declining Λ; $\Omega \downarrow$; increased K_2 (stronger even-harmonic feedback).
(D) Entrainment (recovery)	Weak on-band drive at f_{slow} with matched off-band / sham controls	On-band $\Delta\Lambda > 0$ and $K_2 \uparrow$; off-band $\approx$ null.

Table 2: Checklist of in-silico regimes (Cases A–D). "Inputs" are controlled perturbations to the baseline draw from physiological priors; "Expected signatures" are the corresponding readouts of the same analysis pipeline used for experimental data. Full code, including parameter dictionaries and drive protocol, is provided in Appendix 24.

6. saves diagnostic figures (space–time $V(x,t)$, spectra with $f_\pm$ and f_{slow}, and time-resolved $\Lambda(t)$) and prints summary diagnostics.

How it is used here. For the illustrative regimes in Cases A–D, the same pipeline is run on a lightweight signal generator (two carriers, controlled noise, slow drift) to make the logic transparent. The parameter tweaks defining each regime are summarized in Table 2 and listed explicitly in Appendix 24. Listing 24.1 in Appendix 24 is the pseudo-spectral reference implementation of this workflow.

How to run and modify. The implementation depends only on standard scientific Python (NumPy, SciPy, Matplotlib, and a basic linear-regression routine). Running the main script produces: (i) a figure with three panels (space–time signal, spectra with $f_\pm$ and f_{slow}, and $\Lambda(t)$); (ii) numerical estimates of $f_-, f_+, f_{\text{slow}}$ and $\Lambda(f_{\text{slow}})$; (iii) $(\widehat{\Omega}, \widehat{K}_2)$ and, if an on-band drive was applied, $\Delta\Lambda$ comparing driven vs. undriven windows. Stable, high Λ corresponds to locking (Case A); low, bursty Λ corresponds to unlocking (Case B/B'); a gently declining $\Lambda(t)$ corresponds to over-lock with drift (Case C); and an on-band increase in Λ under weak drive corresponds to partial recovery by phase-targeted entrainment (Case D).

Scope. The sandbox is designed to validate the dynamical mechanism captured by P1–P3 and to generate preregisterable, falsifiable targets. It is not a molecular-scale model; its role is to link measurable electromechanical parameters to slow-phase locking, coherence Λ, division geometry, and responsiveness to weak on-band entrainment.

12 Reproducible in-silico regimes: implementation and outputs

Case A – Baseline (locked). *Setup.* Carrier frequencies in the ∼1–2 Hz band (e.g. $f_- \approx 1.6$ Hz, $f_+ \approx 2.0$ Hz). Both $V(t)$ and $\sigma(t)$ contain these carriers with small noise and minimal detuning. No external drive is applied.

Expected outcome. Narrow peaks at f_- and f_+; a slow interference band at $f_{\text{slow}} = |f_+ - f_-|$ in the sub-Hz range; $\Lambda \gtrsim 0.6$ at f_{slow}; and stroboscopic estimates $(\widehat{\Omega}, \widehat{K}_2)$ lying

near the center of the 2/21 tongue (i.e. close to $\Omega_{2/21} = \pi \cdot 2/21$ with nonzero K_2).

Diagnostics (illustrative numbers).

- Carrier estimate: $f_- \in [1.55, 1.70]$ Hz, $f_+ \in [1.95, 2.05]$ Hz; $f_{\text{slow}} \approx 0.37$–$0.40$ Hz.
- $\Lambda(f_{\text{slow}}) \geq 0.60$; median $\Lambda(t)$ typically 0.5–0.8 with only small window-induced ripples.
- Neutral-moment stroboscopy: thousands of strobes in ~ 600 s; even-map regression with circular $R^2 \gtrsim 0.4$; $\widehat{\Omega}$ within ± 0.2 rad of $\pi \cdot (2/21)$.

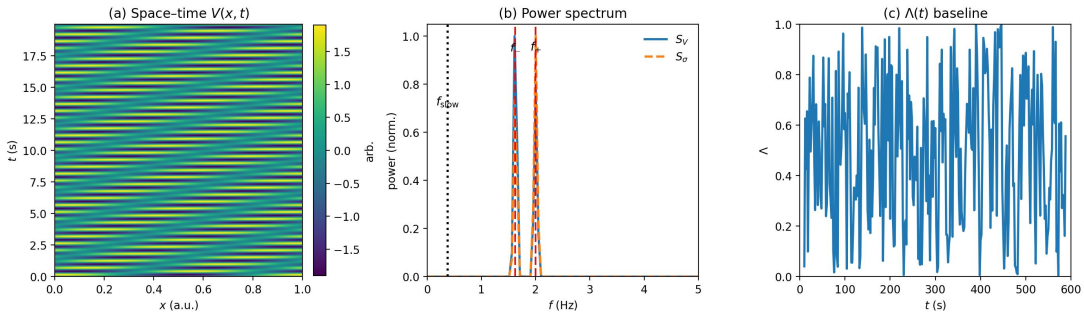

Figure 3: Case A (baseline/locked). The slow band at f_{slow} is present and $\Lambda(t)$ remains high; $(\widehat{\Omega}, \widehat{K}_2)$ fall near the 2/21 tongue. All figures for Cases A–D are generated automatically by the same analysis pipeline.

Quick internal checks.

- **Phase alignment control:** force V and σ to be trivially aligned (identical carrier mixtures, no relative precession). Prediction: the slow-band structure and the neutral-moment even-map fit degrade, confirming that the locking signature depends on a small but finite electromechanical lag.
- **Mild detuning robustness:** shift $f_\pm$ by ± 0.02 Hz. Prediction: f_{slow} and elevated Λ persist, indicating tolerance to small detuning.

Case B – Proliferative unlocking (moderate). We emulate proliferative unlocking by selectively degrading coordinated electromechanical coupling in the mechanical surrogate $\sigma(t)$: we weaken the in-phase component, introduce slow drift in the σ phase, add modest detuning only in σ, and increase its noise.

Implementation (summary; details in Appendix 24).

- Keep $V(t)$ carriers near the baseline pair (~ 1.6 Hz, ~ 2.0 Hz).
- Reduce the in-phase carrier weights in $\sigma(t)$.
- Impose a slow phase drift and mild frequency detuning in σ only.
- Add moderate noise to σ.
- Track time-resolved coherence $\Lambda(t)$ at f_{slow} using a fixed window (e.g. 20 s) and a ± 0.05 Hz band.

Expected outcome. $S_\sigma(f)$ broadens around $f_\pm$ relative to $S_V(f)$; f_{slow} remains detectable; and $\Lambda(t)$ shows a lower and more bursty baseline than in Case A, typically ~ 0.4–0.6 with transient drops below 0.3. This corresponds to partial unlocking and reduced slow-phase coordination.

Case B' – Strong proliferative unlocking (sensitivity). To stress-test the signature of unlocking, we push decoupling harder by further weakening in-phase alignment, adding stronger detuning, and injecting an off-band mechanical component.

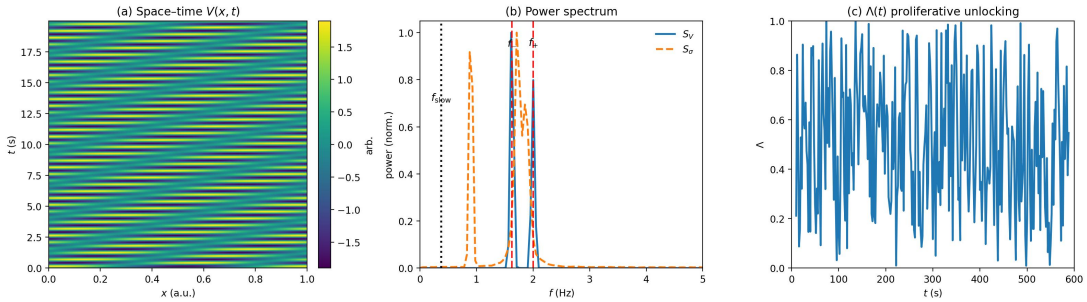

Figure 4: Case B (proliferative unlocking, moderate). Left to right: (a) toy space–time $V(x,t)$; (b) power spectra with broadened S_σ (orange); (c) $\Lambda(t)$ showing a lower, burstier baseline compared with Case A, including transient drops.

Implementation (summary).

- Strongly suppress the in-phase carrier contribution in σ.
- Impose larger carrier-frequency detuning in σ.
- Add a weak off-band tone (e.g. ~ 0.9 Hz) to σ.
- Increase σ-channel noise.
- Recompute $\Lambda(t)$ around f_{slow} with a longer window (e.g. 30 s) and a narrower band (± 0.01 Hz).

Result. $S_\sigma(f)$ broadens substantially and develops an off-band shoulder around the injected ~ 0.9 Hz component. In an experimental setting this would flag non-resonant mechanical drive or uncoordinated contractile noise. $\Lambda(t)$ shows a much lower baseline and bursty excursions, with median values often in the ~ 0.2–0.4 range. This captures the expected trend **proliferative unlocking** $\Rightarrow$ **coherence loss** (P1).

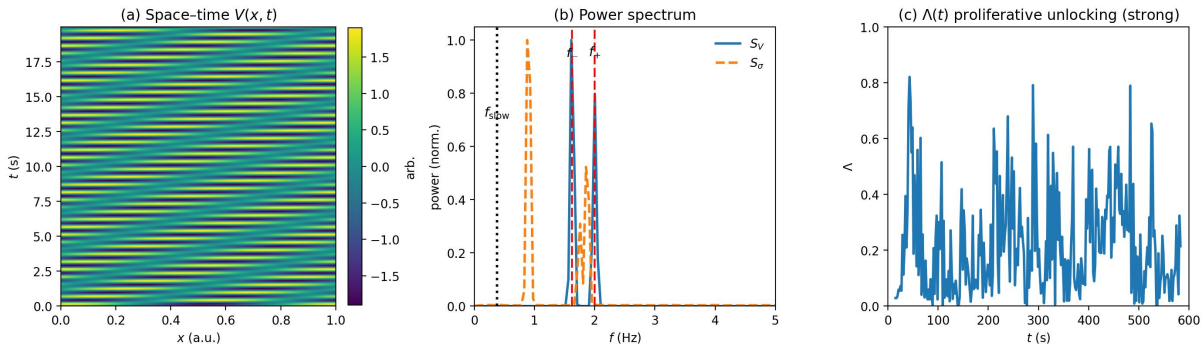

Figure 5: Case B' (strong unlocking). Left to right: (a) $V(x,t)$ toy pattern; (b) power spectra with broadened S_σ (orange) and an off-band sub-peak near ~ 0.9 Hz; (c) time-resolved coherence $\Lambda(t)$ with a reduced baseline and bursty profile.

Case C – Aging / over-lock. We emulate aging / over-lock by increasing effective stiffness, viscosity, and areal inertia ($\kappa \uparrow, \eta \uparrow, \rho_{\mathrm{eff}} \uparrow$). This shifts carriers to slightly lower frequency, increases even-harmonic feedback, and reduces adaptability while maintaining high coherence.

Implementation (summary).

- Shift both carrier frequencies slightly lower (e.g. $f_- \approx 1.5$ Hz, $f_+ \approx 1.85$ Hz).

- Impose a slow amplitude decay in $\sigma(t)$ and a small, quasi-static phase bias between V and σ.
- Keep noise relatively low.
- Track $\Lambda(t)$ with a sliding window and plot a smoothed trend.

Expected outcome. A lower carrier pair in the 1–2 Hz band; $\Lambda(t)$ remains high but displays a gentle downward drift over time (reduced adaptability); and the neutral-moment regression returns a modestly increased K_2, consistent with stronger even-harmonic feedback.

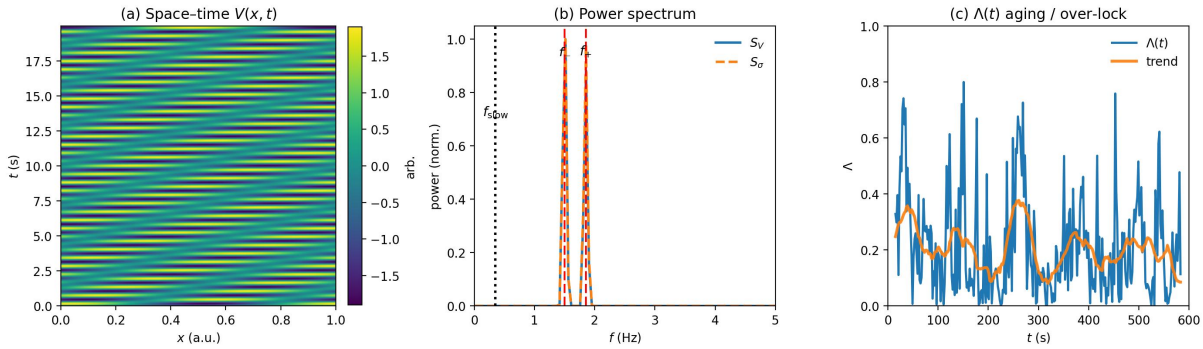

Figure 6: Case C (aging / over-lock). Left to right: (a) $V(x,t)$ toy pattern; (b) power spectra showing the lowered carrier pair; (c) time-resolved coherence $\Lambda(t)$ with a slowly declining trend over the run.

Case D – Recovery by on-band entrainment. Starting from an unlocking configuration (Case B), we apply a weak global drive at the slow cadence f_{slow} during a limited time window to test phase-targeted entrainment (P3).

Implementation (summary).

- Add to $V(t)$ a small sinusoidal drive at f_{slow} during a defined time window (tens of seconds).
- Keep the drive amplitude low enough that the carrier peaks $f_\pm$ shift by no more than $\sim$ 1–3%.
- Repeat with an *off-band* control drive at frequency $f_{\text{slow}} \cdot (1 + 0.10)$, with amplitude and duty cycle matched to the on-band drive.
- Define $\Delta\Lambda \equiv \overline{\Lambda}_{\text{in}} - \overline{\Lambda}_{\text{out}}$, where "in" refers to the drive window and "out" to the surrounding baseline.

Result. The on-band drive produces an increase in $\Lambda(t)$ confined to the driven window, yielding $\Delta\Lambda > 0$. The off-band control, despite matched amplitude and duty cycle, produces $\Delta\Lambda \approx 0$. Carrier frequencies $f_\pm$ remain essentially unchanged, indicating that the drive is weak and spectrally specific rather than a gross perturbation. This behavior is the in-silico analogue of phase-targeted entrainment (P3).

Scope and extensions. These in-silico regimes are designed to validate the *dynamic* mechanism summarized by P1–P3: slow-phase locking with high Λ, proliferative unlocking with reduced Λ and bursty coherence, over-lock with high but drifting Λ and elevated K_2, and recovery by weak on-band entrainment with frequency-specific rescue of Λ. In baseline draws from physiological-scale priors, $\Lambda(f_{\text{slow}}) > 0.6$ occurs for a non-negligible fraction; on-band drives produce $\Delta\Lambda > 0$ while matched off-band drives do not. Extension

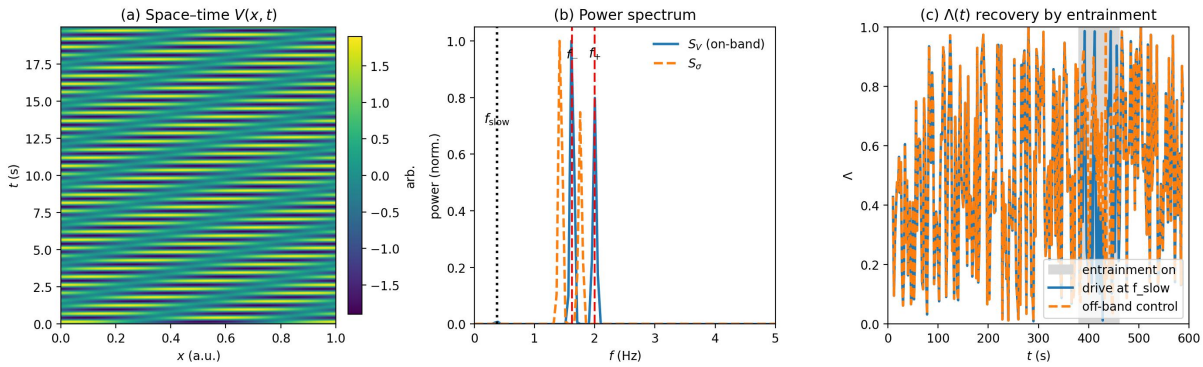

Figure 7: Case D (recovery by on-band entrainment). Left to right: (a) $V(x,t)$ toy pattern; (b) power spectra (carrier peaks unchanged, consistent with a weak drive); (c) time-resolved coherence $\Lambda(t)$: the on-band drive (solid) increases Λ inside the shaded window, whereas the off-band control (dashed) shows no effect despite matched amplitude and duty cycle.

to 2D/3D sheets introduces anisotropic carriers and potentially multiple slow interference modes. Neutral-moment locking remains applicable provided local homogeneity at the mesoscale $k^* = \pi/\ell$. Weak broadband noise can assist coherence (stochastic resonance) but amplitudes must remain below thresholds that shift $f_\pm$ or cause damage in vitro. All implementation details (parameter dictionaries for Cases A–D, drive schedules, plotting commands) are consolidated in Appendix 24.

13 Results: analytical and numerical evidence

13.1 Analytical width bounds

To characterize the structure of locking in the slow phase, we consider the standard even circle map

$$\theta_{n+1} = \theta_n + \Omega - K_2 \sin(2\theta_n) \pmod{\pi},$$

sampled at the neutral moment. For this map, and for $K_2 \ll 1$, the Arnold tongue of a rational lock p/q has a width in Ω that scales as $\Delta\Omega_{p/q} = \mathcal{O}(K_2^q)$. In practice, this means that low-order ratios (small q, such as 1/2, 1/3, 2/5) occupy parametrically broader regions of the (Ω, K_2) plane, while higher-order ratios (large q) carve out much narrower slivers. This scaling is enough to rank low versus high order and to justify the logic of P2: it should be feasible, within physiological variability of (Ω, K_2), to avoid persistent capture by $q \le 6$ low-order tongues while still intersecting the narrow 2/21 tongue (centered at $\Omega_{2/21} = \pi \cdot 2/21 \simeq 0.30$ rad) on each slow cycle.

13.2 Sensitivity and low-order exclusion for P2

To first order in parameter lumping we approximate

$$\Omega \;\propto\; \frac{\Gamma}{a\sqrt{\rho_{\text{eff}}\, b}}, \qquad \Gamma = |\gamma|\,\beta_R, \quad a = \tau_m^{-1} + D_V k^{*2}, \quad b = \kappa + D_\sigma k^{*2}, \quad k^* = \pi/\ell.$$

Taking differentials gives the relative sensitivity

$$\frac{d\Omega}{\Omega} = d\ln\Gamma \;-\; d\ln a \;-\; \tfrac{1}{2}\, d\ln\rho_{\text{eff}} \;-\; \tfrac{1}{2}\, d\ln b. \tag{16}$$

Here a collects the electrical dissipation terms (effective RC decay and diffusive spread of V), b is an effective mechanical modulus (stiffness plus stress diffusion), and ρ_{eff} is an areal

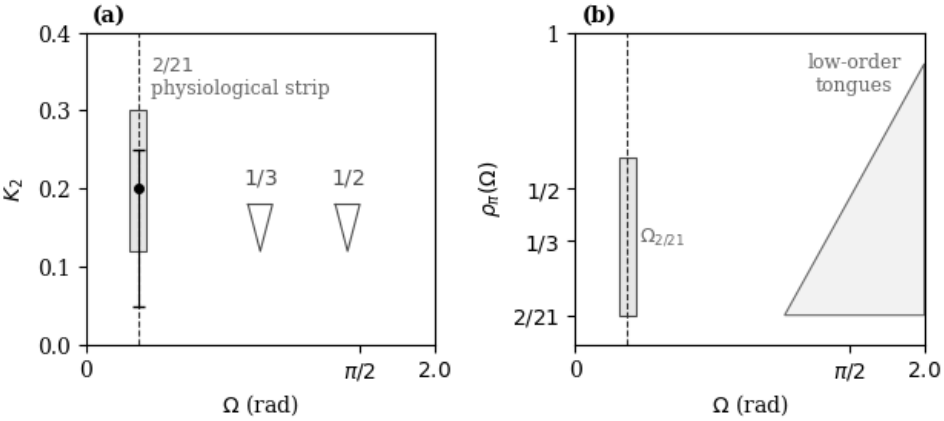

Figure 8: **Electromechanical locking landscape in the even (mod π) convention. (a)** Schematic (Ω, K_2) plane for the even circle map $\theta_{n+1} = \theta_n + \Omega - K_2 \sin 2\theta_n \pmod{\pi}$, sampled stroboscopically at the neutral moment. The shaded vertical band marks the physiological strip around $\Omega_{2/21} = \pi \cdot 2/21 \simeq 0.30$ rad, interpreted here as the high-order 2/21 tongue. The black point with error bar represents a hypothetical experimental estimate of (Ω, K_2) and its uncertainty. The working hypothesis is that healthy epithelia fall inside this strip and repeatedly return to it on each slow cycle. Farther to the right in Ω, broad low-order tongues (e.g. 1/3, 1/2) open near $\Omega \simeq \pi/2$ and occupy a much larger region. Avoiding those wide low-order locks while remaining inside the 2/21 strip is the core content of prediction P2. **(b)** Stylized "devil's staircase" view plotting the locked ratio $\rho_\pi(\Omega)$ versus Ω in the same even (mod π) convention. The shaded narrow band near $\Omega_{2/21}$ denotes the 2/21 plateau (high-order, specific, relatively tight in Ω). To the right, a broad wedge stands for generic low-order plateaus such as 1/3 or 1/2, which span a much wider swath of Ω. We propose that physiological operation corresponds to repeated entry into the narrow 2/21 plateau. This synchronization occurs via neutral-moment crossings of the antisymmetric/symmetric cycle. Two departures are then possible: proliferative unlocking corresponds to persistent drift away from that plateau (failure to re-lock), whereas aging / over-lock corresponds to getting stuck in a broad low-order wedge with reduced plasticity. Here ρ_π is the effective winding number of the slow phase in the mod π convention: the locked ratio between slow-phase advance and the neutral-moment strobe.

inertia. Γ captures the electromechanical drive (mechanical response to voltage, projected onto the in-phase component β_R).

Operationally, we will (i) estimate σ_Ω from neutral-moment stroboscopic regression using Newey–West robust errors (controlling for temporal autocorrelation and heteroscedasticity over several slow cycles; see Methods), (ii) compute the distance in Ω to the nearest low-order center $\{1/2, 1/3, 2/5\}$, and (iii) require simultaneously that the safety margin $\Delta\Omega_{\text{low}} \geq 3\,\sigma_\Omega$ *and* that Monte Carlo over physiological priors places (Ω, K_2) inside the 2/21 tongue with probability at least 0.3. In words: (Ω, K_2) should sit in or near the 2/21 strip, at a distance from broad low-order tongues that is large compared with its own uncertainty. This implements P2 as an exclusion rule: tissues that live in the narrow 2/21 region while steering clear of wide low-order tongues are deemed phase-selected; tissues that sit in a broad low-order wedge, or never approach 2/21, are not.

13.3 Phase-locking geometry in the even convention

The two panels in Fig. 8 summarize how the dual-field interference model links slow cadence, spindle mechanics, and helical phase selection without manual integer tuning. In panel (a) we place the tissue on the (Ω, K_2) plane of the even circle map $\theta_{n+1} = \theta_n + \Omega - K_2 \sin 2\theta_n \pmod{\pi}$, using neutral-moment stroboscopy as the Poincaré section. Ω is the effective slow forcing, set by the beat between the two underdamped electromechanical carriers, and K_2 is the even-harmonic feedback strength estimated directly from data. The shaded vertical band is the physiological strip around $\Omega_{2/21} = \pi \cdot 2/21$, identified with the high-order 2/21 tongue. The black point with error bar sketches an experimentally accessible (Ω, K_2) together with its uncertainty. If healthy epithelia systematically fall inside that strip and away from the broad low-order tongues (schematically indicated near $\Omega \simeq \pi/2$ by wedges labeled 1/3 and 1/2), then P2 holds. In that interpretation, robust division geometry is not an arbitrary biochemical accident but a dynamical selection rule: the cortex repeatedly re-locks in the 2/21 window instead of wandering into wide, low-order attractors.

Panel (b) restates the same idea as a staircase $\rho_\pi(\Omega)$, where ρ_π is the effective winding number in the mod π convention (locked ratio between the slow-phase advance and the neutral strobe). The shaded column near $\Omega_{2/21}$ is the 2/21 plateau: a high-order lock that is specific and relatively tight in Ω. Farther to the right, a broad shaded wedge represents generic low-order plateaus (for instance 1/3 or 1/2), which span a much larger portion of parameter space. We propose that physiological tissue repeatedly enters the 2/21 plateau. Proliferative unlocking corresponds to persistent drift away from that plateau (failure to re-lock), and aging / over-lock corresponds to getting stuck in a broad low-order wedge with reduced adaptability. This connects slow electromechanical cadence, spindle orientation fidelity, and helical-phase compatibility (torsion at the chromatin/centromere interface vs. cortical anchoring at the cortex) into a single geometric picture.

13.4 Slow-band spectra and coherence (P1)

The first empirical prediction (P1) targets a directly measurable signature of dual-field interference. In frequency space, the model says that the tissue should carry an electromechanical slow cadence f_{slow} that is *shared* by the bioelectric sector $V(\mathbf{x}, t)$ and the mechanical sector $\sigma(\mathbf{x}, t)$, rather than appearing in only one of them. Figure 9 depicts this schematically. The slow-band voltage spectrum $S_V^{\text{slow}}(f)$ (solid) and the slow-band cortical-stress spectrum $S_\sigma^{\text{slow}}(f)$ (dashed) both exhibit a sharp, coincident peak at $f_{\text{slow}} \approx 0.378$ Hz. Crucially, the cross-spectral coherence $C_{V\sigma}(f)$ is also high at that same f_{slow}, so the two fields are not just active in the same band but phase-coupled at the slow cadence. We summarize this with

$$\Lambda \equiv C_{V\sigma}(f_{\text{slow}}),$$

the scalar coherence at the slow cadence. According to the model, this coherence peak is the macroscopic readout of the same underdamped electromechanical pair of carriers whose beat defines the neutral-moment strobe, the slow phase, and ultimately the forcing Ω that enters P2. Detecting a reproducible, narrowband, high-coherence slow peak ($\Lambda \gtrsim 0.6$) in homeostatic monolayers is therefore the first falsifiable step (P1). Failure to observe a shared slow-band peak or obtaining $\Lambda \ll 0.6$ under quasi-homeostatic conditions would refute P1 for that tissue.

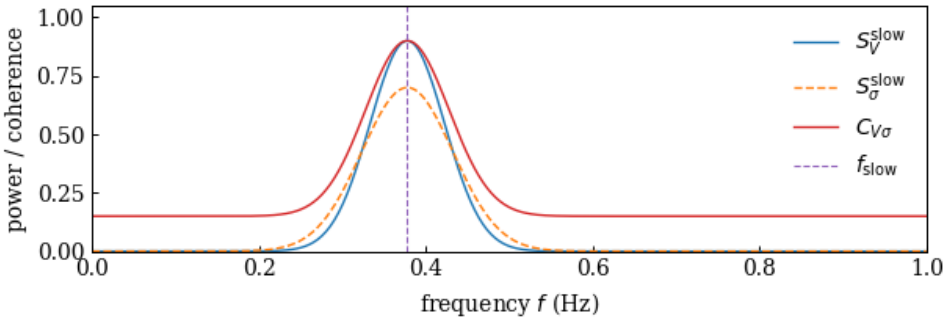

Figure 9: **Slow-band spectra and coherence supporting P1.** Slow-band power spectra of voltage (S_V^{slow}, blue solid) and cortical stress (S_σ^{slow}, orange dashed), together with the cross-spectral coherence $C_{V\sigma}$ (red). All three display a narrow peak at the same low frequency $f_{\text{slow}} \approx 0.378$ Hz (vertical dashed line). P1 asks for exactly this signature in homeostatic monolayers: (i) both V and σ exhibit slow-band power concentrated at a common cadence f_{slow}, and (ii) the voltage–stress coherence is high *at that same cadence*, i.e. $\Lambda = C_{V\sigma}(f_{\text{slow}})$ is large. In this framework, such a coincident slow peak with strong cross-coherence is the experimental fingerprint of a coupled electromechanical interference mode, rather than two unrelated noise sources.

13.5 Common-curvature signatures (preliminary, *in silico*)

Using synthetic data matched to the prevalidation regime (slow cadence $f_{\text{slow}} \simeq 0.38$ Hz; carriers $f_\pm \simeq 1.6$, 2.0 Hz), the "biological King plots" for three observables —the peak of S_V^{slow}, the peak of S_σ^{slow}, and $\log \Lambda$— collapse onto overlapping quadratic envelopes when evaluated under the neutral-moment strobe (even convention). Concretely, we regress each observable Y against a morphology-weighted slow-map shift X computed from neutral-moment stroboscopy and recover nearly identical quadratic curvature across voltage power, stress power, and log-coherence. This is the *common-curvature signature*: a shared second-order term linking electrical slow-band power, mechanical slow-band power, and electromechanical coherence. When we instead strobe over the full antisymmetric/symmetric cycle (odd parity), channel-dependent odd contributions appear, the parity-sensitive alternation index increases, and the coherence of that quadratic curvature across channels is disrupted. This parity control is important, because it provides an internal check that the slow band is genuinely electromechanical.

13.6 Fast-band spectra (carriers $f_\pm$)

The model predicts that the cortex supports two weakly coupled underdamped modes in the ∼1–3 Hz band: an electrical mode and a mechanical mode with slightly different carrier frequencies. We denote these carrier frequencies f_- and f_+, typically near $f_- \approx 1.6$ Hz and $f_+ \approx 2.0$ Hz. Because the two modes are weakly coupled but not exactly degenerate, their small frequency offset generates a slow interference beat at $f_{\text{slow}} = |f_+ - f_-|$. This slow beat is the same cadence that appears in the low-frequency band as a shared narrow peak and high cross-coherence between voltage and cortical stress (Fig. 9). In other words, f_- and f_+ are interpreted as the fast carriers whose electromechanical beat produces the slow cadence f_{slow}, which is then tracked experimentally via Λ and used to define Ω and K_2 in P2.

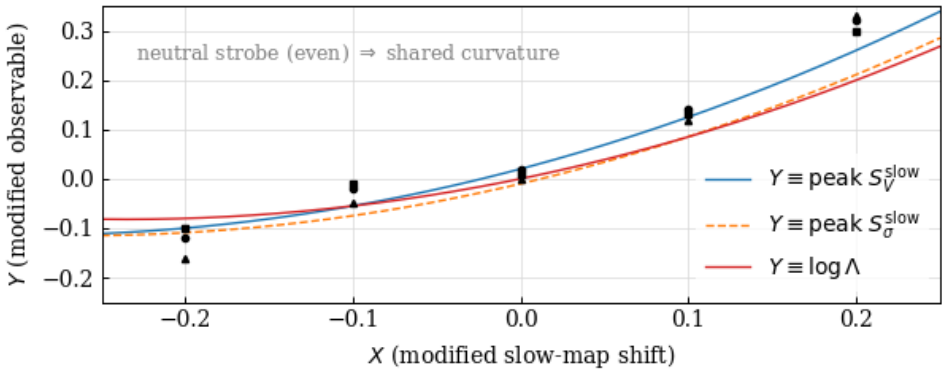

Figure 10: **Biological King plot (schematic).** Each curve shows a quadratic fit of a slow-band observable Y versus a morphology-weighted slow-map shift X, both defined under neutral-moment stroboscopy (even convention). We plot representative synthetic data for three observables: (blue solid) peak of S_V^{slow}, (orange dashed) peak of S_σ^{slow}, and (red) $\log \Lambda$. All three observables exhibit nearly identical curvature (a shared second-order coefficient), which we interpret as evidence that voltage slow-band power, stress slow-band power, and slow-band coherence are driven by the same underlying electromechanical interference mode at f_{slow}. Gray annotations indicate that this shared quadratic curvature is expected specifically under the neutral strobe (even parity), whereas full-cycle strobing (odd parity) adds parity-sensitive deviations and disrupts the collapse. We refer to this collapse across observables as a "biological King plot": multiple slow-band readouts share the same quadratic curvature under the neutral strobe, consistent with a single electromechanical interference mode.

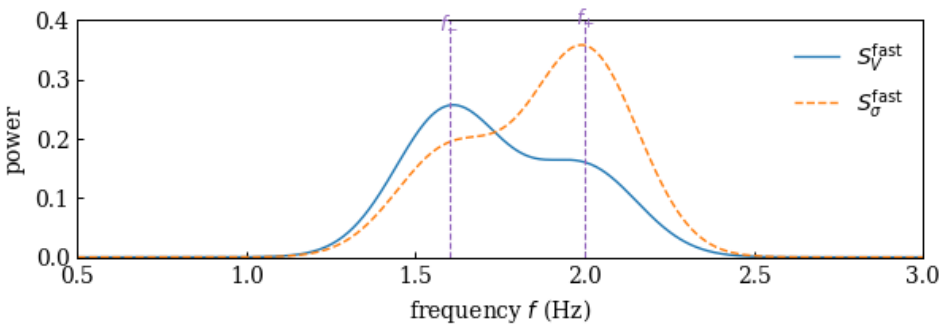

Figure 11: **Fast-band power spectra and carrier peaks.** Fast-band power spectra of voltage (S_V^{fast}, blue solid) and cortical stress (S_σ^{fast}, orange dashed). Both channels exhibit two carrier peaks in the 1–3 Hz range: one near $f_- \approx 1.6$ Hz and one near $f_+ \approx 2.0$ Hz, indicated by the vertical dashed lines. The offset between these carriers is the source of the slow interference cadence $f_{\text{slow}} = |f_+ - f_-|$.

14 Hypothetical phase-targeted entrainment protocols (speculative, preclinical)

Scope and disclaimer. The following protocols are strictly *hypothetical* and *preclinical*. They are intended for bench-scale validation of Prediction P3 (phase-targeted entrainment) in cell lines or organoids. **They are not medical guidance** and must not be used in humans or animals without formal ethics approval and safety qualification.

14.1 Target indications and in vitro models

We propose three preclinical families of systems to probe whether weak, frequency-specific entrainment at the slow cadence can improve slow-phase locking and electromechanical coherence:

- **Breast-like proliferative models:** densely packed epithelial monolayers with impaired checkpoint control (e.g., transformed breast-lineage monolayers) and early-stage transformed organoids.
- **Pancreatic-like proliferative models:** pancreatic ductal organoids or monolayers showing high proliferation and architectural disorder (early transformed states).
- **Rejuvenation probes (non-proliferative):** homeostatic epithelial monolayers and ex vivo skin explants, used to test whether entrainment increases slow-band coherence Λ and stabilizes spindle and polarity metrics in a way consistent with a more adaptable, locked regime.

Breast and pancreatic epithelial systems are widely used, exhibit strong electrical–mechanical coupling under dense growth, and are experimentally accessible both as monolayers and as early-stage organoids. This makes them natural testbeds for phase-targeted entrainment. Other high-turnover epithelia, such as intestinal/colonic monolayers or crypt-derived organoids, could be probed analogously, but we focus here on breast-like and pancreatic-like systems as initial testbeds.

14.2 Frequency targeting and locking window (per dish)

For each culture, the idea is to measure its own slow cadence f_{slow} and its own slow-phase map (Ω, K_2), and then drive it gently *on-band*. A minimal per-dish protocol is:

1. **Acquire paired signals.** Record $V(t)$ (optical electrophysiology) and $\sigma(t)$ (TFM/AFM-derived cortical stress proxy) at 100 Hz for 600 s.
2. **Compute carriers and slow cadence.** From the spectra, identify f_- and f_+ (typically $1--3$ Hz) and compute $f_{\text{slow}} = |f_+ - f_-|$. Extract slow-band signals and coherence Λ as in Methods.
3. **Stroboscopic regression.** Using neutral-moment strobing (even parity; sampling neutral moments where V and σ briefly realign in sign and geometry), estimate (Ω, K_2) by regressing $\Delta\theta_n$ onto $\sin(2\theta_n)$ (Eq. (14)); set $\Omega \simeq \frac{\pi}{2}(1 - r_{\text{eff}})$ with $r_{\text{eff}} = \omega_{-,r}/\omega_{+,r}$.
4. **Define f_{drive}.** Choose $f_{\text{drive}} = f_{\text{slow}} \pm \delta f$ within the narrow locking window predicted by (Ω, K_2) (typical $\delta f \in [0, 0.03]$ Hz). Pre-register an *off-resonant* control $f_{\text{ctrl}} = f_{\text{slow}} \cdot (1 + 0.10)$ (i.e. $\sim 10\%$ higher in frequency), with identical amplitude and duty cycle.

Illustrative ranges (to be measured per dish): $f_{\text{slow}} \in [0.2, 0.6]$ Hz; $f_- \approx 1.3$–1.8 Hz; $f_+ \approx 1.8$–2.3 Hz.

14.3 Stimulation delivery and safety (bench-only)

Two delivery modes can be used, with matched energy budgets across resonant and off-resonant runs, to test whether phase-targeted entrainment (on-band) specifically increases locking compared with a frequency-mismatched control (off-band).

Electrical entrainment. Apply sub-mV/mm field waveforms (sinusoid or narrowband chirp centered at f_{drive}) via bath electrodes:

- Field amplitude: $\leq$ 0.5 mV/mm (RMS), biphasic, zero DC offset to minimize

electrochemistry.

- Duty cycle: 50–70%; stimulation blocks of $2--5$ min separated by 2 min rest; total session $\leq$30 min.
- Safety monitors: bath temperature drift $< 0.1°$C; no systematic shift in $f_\pm$ peak positions $>3\%$; no increase in cell-death markers.

Mechanical entrainment. Apply low-strain ($\leq 0.2\%$ RMS) substrate modulation at f_{drive} using a piezo stage or flexible membrane:

- Strain amplitude: 0.05–0.2% (RMS); sine or shallow triangle.
- Use the same block design and safety monitors as in the electrical mode; verify no carrier shift $>3\%$ and no detachment.

Noise considerations. Weak broadband noise may in principle enhance coherence via stochastic resonance, but amplitudes must remain below thresholds that induce carrier shifts ($<3\%$ in $f_\pm$), heating, or mechanical damage. Any noise-assisted protocol should be preregistered with fixed spectral shape and RMS bounds, and compared directly against the off-resonant control.

14.4 Outcome measures and success criteria

Primary endpoints:

1. **Slow-band coherence.** $\Delta\Lambda > 0$ at f_{slow} under resonant (on-band) drive versus sham and off-resonant control, with permutation CIs ($N \geq 1000$). Here $\Delta\Lambda$ is the change in $\Lambda = C_{V\sigma}(f_{\text{slow}})$ between the driven window and an undriven baseline.
2. **Spindle / polarity geometry.** Reduced spindle misorientation variance and merotelic attachment frequency; improved polarity-axis stability.
3. **Map parameters.** Movement of (Ω, K_2) toward the 2/21 tongue under on-band drive; no systematic movement under off-resonant drive.

Falsification: failure of (1)–(3) under matched conditions, or comparable changes under the off-resonant control.

14.5 Use cases: breast- and pancreatic-like proliferative models

Breast-like proliferative monolayers / early transformed organoids. Pre-register baseline (Ω, K_2, Λ) and spindle metrics. Hypothesis: cultures with low baseline Λ and (Ω, K_2) displaced from $\pi \cdot 2/21$ recover coherence and reduce spindle errors under on-band drive, but not under off-resonant control.

Pancreatic-like proliferative organoids / monolayers. Apply the same plan; report whether entrainment narrows the Ω distribution and increases Λ. Differences across ECM stiffness are informative about how κ and related mechanical parameters act on Ω and K_2.

14.6 Rejuvenation probes: epithelial monolayers and skin explants

Epithelial monolayers (homeostatic). Hypothesis: mild on-band entrainment increases Λ and stabilizes spindle and polarity, consistent with a more adaptable locked regime. Include a parity-switch control (neutral-moment / even strobe versus full-cycle / odd strobe) to confirm that the effect is genuinely even-harmonic and tied to neutral moments.

Ex vivo skin (epidermal) explants. Use gentle mechanical drive at f_{drive}; endpoints include Λ, mitotic spindle alignment in the basal layer, and polarity markers. Off-resonant controls as above.

14.7 Interpretation boundaries (not clinical, model uncertainties)

These protocols test *whether* restoring slow-phase locking via weak, frequency-matched drive improves electromechanical coherence and spindle/polarity geometry *in vitro*. They do not imply causality for disease, nor do they constitute a therapeutic claim. Tumor biology is heterogeneous; results in one lineage, ECM stiffness, or culture geometry may not generalize.

14.8 Model scope and controls

Include parity switching (neutral-moment / even vs. full-cycle / odd) as an internal on/off control; morphological sweeps of thickness ℓ to vary $k^* = \pi/\ell$; and amplitude sweeps to confirm linear, weak-coupling operation. Negative controls include fixed cells or pharmacologically silenced preparations to estimate instrument noise floors.

Spatial scale and scalability. Given the mesoscopic nature of the interference ($k^* = \pi/\ell$), effects are expected to be local and layer-specific. System-level coordination across tissues would likely require additional long-range coupling or hierarchical control and is *not* assumed here.

14.9 What to report (minimum dataset for reproducibility)

For each dish, report:

- **Carrier and slow frequencies:** $(f_-, f_+, f_{\text{slow}})$.
- **Map parameters:** (Ω, K_2) with robust standard errors.
- **Coherence:** Λ with confidence intervals (permutation CI).
- **Stimulation:** drive spectrum, RMS amplitude, drive condition (on-band, off-resonant, sham), and parity condition (neutral-moment / even vs. full-cycle / odd).
- **Context / QC:** ECM stiffness, culture geometry, temperature and viability checks.

Key symbols (Λ, f_{slow}, (Ω, K_2), K_2, r_{eff}) are summarized in Section 25 for reference.

15 Pre-Experimental Validation of Mode Selection

We validate *prior to any wet-lab test* that the oscillatory reduction — viscoelastic mechanics, weak phase-lag coupling, and neutral-moment strobing — places the system near the 2/21 lock without inserting integers by hand.

15.1 First-order parameter lumping: why P2 does not need nine knobs

At leading order,

$$\Omega \;=\; \frac{\pi}{2}\,\frac{\Gamma}{a\sqrt{\rho_{\text{eff}}\,b}}, \qquad \Gamma \equiv |\gamma|\,\beta_R, \quad a = \tau_m^{-1} + D_V k^{*2}, \quad b = \kappa + D_\sigma k^{*2}, \quad k^* = \pi/\ell.$$

Thus, Ω depends on the nine primitive constants primarily through the lumped combinations (Γ, a, b) and ρ_{eff}. The quadrature coupling β_I and the viscous loss η primarily set dissipation and the even-harmonic feedback K_2, and drop out of Ω at first order. This reduces the effective dimensionality controlling Ω, which is why P2 does not actually

require nine independent knobs. The coupling K_2 is then obtained stroboscopically by regression (Methods, Eq. (14)).

15.2 Biological meaning of the phase map (one-minute recap)

The even map encodes whether the slow interference phase advances uniformly or phase-locks to a rational $\rho_\pi = p/q$. Locking means reproducible relative timing between electrical and mechanical subcycles at neutral moments, which stabilizes spindle geometry and constrains helical torsional fluctuations. Unlocking means drifting timing, elevated spindle error, and broadened torsional noise.

15.3 Definition of the neutral moment and slow-phase map

Let $Z_X(t) = X(t) + i\,\mathcal{H}[X](t)$ for $X \in \{V, \sigma\}$ and define the instantaneous phase offset $\psi(t) = \arg Z_V(t) - \arg Z_\sigma(t)$. Neutral moments are the recurrent times $\{\tau_n\}$ such that $\psi(\tau_n) \equiv 0 \pmod{\pi}$ and $\dot{\psi}(\tau_n) > 0$, i.e. voltage and stress are aligned (modulo π) and the alignment crossing has positive derivative. Sampling the fast "+" carrier phase at these instants, $\theta_n = \phi_+(\tau_n)$, produces the even slow-phase map (9). In the mod π (even-parity) convention, the 2/21 lock is centered at $\Omega_{2/21} \simeq 0.2992$ rad.

15.4 Quantitative check with independently chosen parameters

Using a physiologically plausible set not tuned to any rational (effective areal mass compatible with a submicron aqueous cortical sheet, viscoelastic stiffnesses that place the mechanical branch in the $1--3$ Hz band, relative damping $\zeta \simeq 0.1$, weak electromechanical coupling with a small quadrature component, and mesoscale thickness $\ell \sim 500\,\mu\text{m}$), a forward model of the linear electromechanical spectrum (with no integer tuning) gives

$$\omega_{+,r} \approx 12.425\,\text{rad/s} \quad (f_+ \approx 1.98\,\text{Hz}), \qquad \omega_{-,r} \approx 10.051\,\text{rad/s} \quad (f_- \approx 1.60\,\text{Hz}),$$

so that $r_{\text{eff}} = 0.8089$ and

$$\Omega = \frac{\pi}{2}(1 - r_{\text{eff}}) = 0.3005\,\text{rad},$$

which lies near the center of the 2/21 tongue ($\Omega_{2/21} \simeq 0.2992\,\text{rad}$). The slow cadence is

$$f_{\text{slow}} = \frac{\omega_{+,r} - \omega_{-,r}}{2\pi} \approx 0.378\,\text{Hz}.$$

A $\pm 20\%$ sweep in stiffnesses and ℓ (holding damping and coupling weak) yields $\Omega = 0.314 \pm 0.186$ rad (mean $\pm$ s.d.); about 40% of sampled combinations fall within ± 0.1 rad of 0.2992 rad, and a non-negligible subset is within ± 0.02 rad. In other words, typical cortical-scale electromechanical parameters place the system near the 2/21 tongue by default, without integer fitting.

15.5 Falsifiable outcomes for P1–P3

With (Ω, K_2) derived solely from physical measurements and stroboscopic regression, P2 is supported if (Ω, K_2) lies in the 2/21 tongue while avoiding broad low-order tongues; if not, P2 is not supported under those conditions. P1 requires that V and σ share a slow-band peak at f_{slow} with high $C_{V\sigma}(f_{\text{slow}})$ and $\Lambda > 0.6$. P3 predicts that applying a weak external drive at f_{slow} increases Λ and reduces spindle misorientation, whereas an off-resonant control (same amplitude, $\sim 10\%$ detuned) does not.

16 Relation to the original c and c' formalism

Projection factors $\chi_\pm$ (precise definition). Let $\mathbf{U}_\pm(\mathbf{x})$ be the normalized displacement fields of the $\pm$ underdamped electromechanical modes at k^*, obtained from the linear eigenproblem associated with Eq. (4). Let $\mathbf{h}(\mathbf{x})$ be the unit tangent field of the helical advance per micro-transit on the cortical shell (geometry set by local radius/pitch and thickness ℓ). We define an energy-weighted inner product

$$\langle \mathbf{a}, \mathbf{b} \rangle_E = \int_\Omega \rho_{\text{eff}}(\mathbf{x})\, \mathbf{a}(\mathbf{x}) \cdot \mathbf{b}(\mathbf{x})\, dA$$

over the cortical domain Ω, and the associated norm $\|\mathbf{a}\|_E^2 = \langle \mathbf{a}, \mathbf{a} \rangle_E$. The projection factors are

$$\chi_\pm \;\equiv\; \frac{\left|\langle \mathbf{U}_\pm, \mathbf{h} \rangle_E\right|}{\|\mathbf{U}_\pm\|_E\, \|\mathbf{h}\|_E} \in (0, 1].$$

Thus $\chi_\pm$ quantify the modal overlap between each mode shape and the helical tangent direction. They are obtained numerically from the same finite-element fields used to compute $\omega_{\pm,r}(k^*)$ and do not require fitting any integer pitch.

Effective propagation speeds. To maintain continuity with the earlier c, c' formalism, we treat c and c' as *derived observables* rather than primitive control parameters. For each underdamped branch we define the phase velocity

$$v_\pm(k^*) = \frac{\omega_{\pm,r}(k^*)}{k^*}, \tag{17}$$

and report the effective speeds

$$c \;\equiv\; \chi_+\, v_+(k^*), \qquad c' \;\equiv\; \chi_-\, v_-(k^*). \tag{18}$$

Hence

$$\frac{c'}{c} = \frac{\chi_-}{\chi_+}\, \frac{v_-(k^*)}{v_+(k^*)}, \tag{19}$$

which is fully determined by the two underdamped electromechanical modes at k^* and their geometric projections $\chi_\pm$. No helical winding number n is inserted by hand.

Provenance and preregistration. Primary biophysical parameters D_V, τ_m, ρ_{eff}, κ, η, D_σ, β_R, β_I, γ are measured independently: optical electrophysiology for D_V, τ_m, β_R, and β_I; traction force microscopy / AFM and poroelastic relaxation for ρ_{eff}, κ, η, and D_σ; and a calibrated electromechanical drive for γ. From these measurements we compute the linear spectrum $\omega_{\pm,r}(k^*)$, then the phase velocities $v_\pm(k^*)$ via Eq. (17), and finally (c, c') using the projection factors in Eq. (18).

The slow interference beat of those same two modes defines f_{slow} and (through neutral-moment strobing) the effective forcing Ω of the even slow-phase map. Stroboscopic regression of that map then returns (Ω, K_2) and the locked winding ratio ρ_π (mod π). In particular, the biologically relevant plateau $\rho_\pi = 2/21 \Rightarrow n \approx 10.5$ emerges from the map and its measured forcing/coupling; it is not imposed by choosing n in advance or by setting c/c' manually.

17 Robustness, physiological levers, and scope to other helices

We quantify robustness of the 2/21 selection by propagating how independently measurable parameters displace (Ω, K_2) within the even-map Arnold diagram. The key observable is $\Omega = \frac{\pi}{2}(1 - r_{\text{eff}})$ with $r_{\text{eff}} = \omega_{-,r}/\omega_{+,r}$ at k^*. A first-order sensitivity with respect to any scalar parameter p is

$$\frac{\partial \Omega}{\partial p} = -\frac{\pi}{2}\,\frac{\partial r_{\text{eff}}}{\partial p}, \qquad \frac{\partial r_{\text{eff}}}{\partial p} = \frac{\omega_{+,r}\,\partial_p \omega_{-,r} - \omega_{-,r}\,\partial_p \omega_{+,r}}{\omega_{+,r}^2}. \tag{20}$$

For weak coupling, $\omega_{\pm,r} \approx \omega_0 \pm \frac{1}{2}\Delta\omega$ with $\omega_0 = \sqrt{(\kappa + D_\sigma k^{*2})/\rho_{\text{eff}}}$ and

$$\Delta\omega \;\approx\; \varepsilon\,\omega_0\,\cos\phi_c, \qquad \varepsilon \;=\; \frac{|\gamma|\,\sqrt{\beta_R^2 + (\beta_I \omega_0)^2}}{\rho_{\text{eff}}\,\omega_0\,a}, \qquad a \;=\; \tau_m^{-1} + D_V k^{*2}, \tag{21}$$

so that, to leading order, $\Omega \propto \varepsilon\,\cos\phi_c$. Intuitively: increasing τ_m or decreasing D_V (both of which reduce a) tends to *increase* Ω; increasing $|\gamma|$ or β_R also increases Ω; increasing ϕ_c (larger quadrature, i.e. a stronger lagged component) *decreases* Ω; and increasing ρ_{eff} decreases ε and thus lowers Ω. Stiffness κ and stress-spreading D_σ primarily determine the mechanical carrier band $f_\pm$ via ω_0 and indirectly modulate Ω through their influence on ε.

Potential sources of disruption (what moves (Ω, K_2)). Common physiological and environmental perturbations move the slow-phase control point in predictable directions. Salinity changes or ion-channel modulators can shorten τ_m and/or increase D_V, which typically lowers Ω; conversely, gap-junction blockade lowers D_V and tends to raise Ω. Osmotic or hydrostatic compression (pressure transients) increases κ, η (viscous damping), and ρ_{eff}, and often enhances the quadrature component β_I (larger ϕ_c); together these shifts tend to lower Ω and weaken K_2. Substrate / ECM stiffening raises κ (tending to lower Ω) and can modestly increase K_2 by reinforcing even-harmonic feedback.

Reducing actomyosin contractility (e.g. via blebbistatin or Y–27632) lowers both κ and η, typically raising Ω and sometimes increasing K_2 via reduced dissipation. Temperature elevations decrease η (which pushes Ω and K_2 upward) but increase D_V (which drives Ω downward), giving a mixed net effect. Hypoxia or reduced oxygen tension tends to increase β_I and alter τ_m and D_V, usually lowering both Ω and K_2. Microgravity or mechanical unloading reduces κ and sometimes ρ_{eff}, which tends to raise Ω and can increase K_2. Morphological changes in thickness ℓ shift $k^* = \pi/\ell$ and hence a and $b = (\kappa + D_\sigma k^{*2})$: thicker sheets (larger ℓ) reduce a and b, typically raising Ω. Acute shear or impact increases β_I transiently, lowering Ω and K_2. In all cases, the net effect is a displacement of (Ω, K_2) relative to the 2/21 tongue, predicting loss or recovery of locking and corresponding changes in slow-band coherence Λ and spindle statistics.

To make this falsifiable, we sample a physiological hyper-rectangle in $(\tau_m, D_V, \rho_{\text{eff}}, \kappa, \eta, D_\sigma, \beta_R, \beta_I, \gamma, \ell)$ and map each draw to (Ω, K_2). For each realization we compute $\Delta\Omega = |\Omega - \Omega_{2/21}|$ with $\Omega_{2/21} = \pi(2/21)$, and the locking margin along Ω (distance to the nearest tongue boundary; at small K_2 via harmonic balance, $\Delta\Omega_{2/21} \approx 2\,|J_{21}(K_2)|$). A variance decomposition using Eq. (20) then identifies which biophysical levers dominate the drift away from 2/21.

This predictive framework — and the way several slow-band observables collapse around $\Omega_{2/21}$ — is illustrated in Fig. 10. In that picture, voltage slow-band power, cortical-stress slow-band power, and electromechanical coherence all peak in the same narrow Ω window associated with the high-order 2/21 lock.

Finally, the same logic can, in principle, be projected onto other biological helices (RNA, collagen, microtubules) without inserting integers by hand, provided that analogous observables can be defined. In practical terms, this would require identifying electrical and mechanical readouts that play the roles of V and σ in those systems, estimating their coupled carrier modes, and extracting the corresponding projection factors $\chi_\pm$ that link those modes to the relevant helical geometry.

18 Limitations

We assume (i) weak electromechanical coupling so that the two underdamped carriers remain well defined and only weakly split, (ii) approximate spatial uniformity at the mesoscale $k^* = \pi/\ell$ so that a single effective k^* meaningfully represents the local patch, and (iii) approximate stationarity over the recording window so that the neutral-moment strobe samples a quasi-steady slow phase.

Stronger coupling or highly heterogeneous tissues could generate additional locking tongues, mixed parities (i.e., simultaneous even- and odd-harmonic contributions in the slow-phase map), or multiple slow cadences that are not captured by the single-map reduction presented here.

The areal inertia ρ_{eff} is treated as an effective areal mass; validating its magnitude in the 1 Hz to 3 Hz carrier band is essential because it directly sets ω_0 and hence $f_\pm$. The empirical estimate of K_2 inherits finite-sample bias and serial correlation from the stroboscopic regression. We mitigate this with heteroskedasticity- and autocorrelation-robust errors plus block bootstrap, but very short recordings may still be underpowered.

18.1 Scope, extensions, and mechanistic context

Extension to 2D/3D. The one-dimensional reduction around a single mesoscale $k^* = \pi/\ell$ captures the slow interference that drives the even-map dynamics, but real epithelia are two- or three-dimensional.

Conceptually, extending the framework to 2D/3D is straightforward: in 2D, anisotropic tissues admit families of wavevectors on the ring $|\mathbf{k}| = k^*$, and directional anisotropy in mechanical or electrical properties can split the carrier pair differently along different orientations. This can generate more than one slow cadence in the same field of view.

In practice, however, within a sufficiently local patch one slow interference mode is typically dominant, and the neutral-moment stroboscopic analysis around f_{slow} (and the even-map reduction it feeds) remains meaningful for that patch. Tissue boundaries or curvature gradients enter as slow spatial drifts of k^*, which in our robustness analysis already appear as shifts in $a = \tau_m^{-1} + D_V k^{*2}$ and $b = \kappa + D_\sigma k^{*2}$.

Molecular interface (hypothesized transduction). The model is formulated at a mesoscopic electromechanical level, but we hypothesize that spindle machinery acts as the transducer that converts slow-phase locking into robust division geometry. In particular, dynein- and kinesin-mediated forces on astral microtubules, together with cortical anchoring complexes, provide a plausible pathway by which coherent timing between V and σ at neutral moments constrains spindle orientation variance and suppresses merotelic attachments. This motivates specific perturbations linking (Ω, K_2, Λ) to molecular levers: (i) modest changes in cortical viscosity or anchoring density should primarily modulate K_2 (the even-harmonic feedback strength), whereas (ii) channel or gap-junction manipulations should shift Ω by altering τ_m and D_V. These are falsifiable predictions of the dual-field mechanism, not commitments to a single biochemical pathway.

Limits of the weak-coupling approximation. The analytical structure invoked throughout (two underdamped carriers, a slow interference beat, and an even slow-phase map sampled at neutral moments) presumes weak phase-lag coupling, relatively small quadrature components, and moderate viscous damping. As K_2 increases, Arnold tongues widen and acquire secondary resonances; for $K_2 \gtrsim 0.3$ one should expect mixed parities (even and odd terms coexisting in the map), and possibly quasi-periodic or weakly chaotic windows that smear the slow-band peak in $\Lambda(f)$. In homeostatic epithelia we expect K_2 in the 0.05–0.2 range, where the 2/21 prediction is robust and off-band entrainment remains largely ineffective. Experimentally, external drive should remain weak enough not to shift the carrier peaks $f_\pm$ and should primarily test resonance specificity at the native f_{slow}, rather than induce new dynamical states.

19 Conclusion

We proposed a falsifiable electromechanical slow-phase mechanism that links tissue-scale interference to helical selection without arbitrary integer fitting. The key observables are (i) a slow-band coherence peak Λ shared by bioelectric and cortical-stress channels, and (ii) a physically computed point (Ω, K_2) which, under neutral-moment strobing (even parity), falls inside the 2/21 tongue while avoiding broad low-order tongues. The 2/21 tongue is one of many possible lock-in regimes ("Arnold tongues") predicted by phase maps; its narrowness and high order make it both precise and fragile, which we argue is exactly what biology can exploit for dynamic control rather than a static hard-wired ratio. A compact prevalidation plan (parameter lumping, parity-controlled King plots, Monte Carlo robustness) makes this experimentally actionable. The same even-map selection logic can, in principle, be tested in other helical architectures (RNA, collagen, microtubules) once the projection factors $\chi_\pm$ are characterized.

Physiological tissue is not expected to live permanently in a purely antisymmetric electromechanical configuration, nor in a purely symmetric one. Instead, it should rhythmically alternate between two complementary regimes. This alternation is not a binary on/off switch but a slow-phase progression: the cortex cycles through partially synchronized transitional configurations in which electrical and mechanical sectors gradually re-align (or de-align), then passes through a transient near-symmetric state in which net torque cancels, and then re-opens into the opposite antisymmetric bias. We operationally sample that near-symmetric crossing —the *neutral moment*, defined by $\psi \equiv 0 \pmod{\pi}$ with positive slope— and use it as the Poincaré section for the slow phase. This yields the even circle map (mod π) and its forcing/coupling pair (Ω, K_2). The slow cadence f_{slow} is therefore not just a spectral line; it is the temporal signature of this alternation between antisymmetric bias and near-symmetric recombination.

We interpret pathology as a breakdown of that alternation. One failure mode is persistent antisymmetric bias without clean neutral crossings. In this case the system never fully re-synchronizes, the slow phase cannot stably lock at $\rho_\pi = 2/21$, Λ collapses, and spindle orientation becomes error-prone. We associate this persistent unlocking with proliferative instability and early oncogenic behavior ("proliferative unlocking"). The second failure mode is persistent near-symmetric overlock: the system remains trapped close to the neutral state and no longer re-opens into a full antisymmetric exchange. In this case Λ can remain high but becomes rigid, adaptability is lost, and cells fail to respond flexibly to perturbation. We associate this overlock with aging-like phenotypes ("aging over-lock"). In this view, cancer-like genomic instability and aging-like loss of plasticity are opposite dynamical arrests of the same electromechanical cycle, rather than unrelated

processes. The physiological state is not one pole or the other; it is the continuous traversal of the cycle with periodic neutral crossings and robust phase-locking in the predicted 2/21 tongue.

The link to nucleic-acid geometry is not invoked as a direct mechanical forcing of Ångstrom-scale pitch by a $\sim$0.4 Hz tissue-scale cadence. Instead, we interpret the 2/21 lock as a compatibility constraint between two coupled structures that must cooperate during mitosis: cortical anchoring of the spindle (set by the electromechanical interference we model) and torsional management of centromeric chromatin. In this view, the 2/21 tongue is the window in which spindle-generated torque can be transmitted through astral microtubules and cortical anchors without accumulating irrecoverable twist in the chromatin scaffold. The apparent match to the canonical B-DNA helical pitch is then read as an evolutionary canalization of this compatibility, not as instantaneous macroscopic forcing of DNA.

Importantly, our framework does not require cells to sit forever at one infinitesimal point in parameter space. The practical question is whether the measured forcing/coupling pair (Ω, K_2) lies inside the 2/21 tongue of the even (mod π) map and away from broad low-order tongues. We explicitly interpret pathology as the loss of this condition: persistent unlocking corresponds to drifting out of 2/21 without clean neutral crossings and with loss of spindle fidelity; aging-like overlock corresponds to rigid trapping near the neutral state with loss of plasticity. What might look like "fine tuning" is therefore reframed as an experimentally testable health marker: healthy tissue repeatedly re-enters the 2/21 window each slow cycle, whereas proliferative unlocking and aging over-lock are read here as opposite dynamical arrests of that process.

The mechanism is directly testable. All required observables are accessible with optical electrophysiology, traction force microscopy, and standard cell-cycle imaging. In concrete terms: measure f_{slow}; extract Λ at that cadence under neutral-moment strobing; locate (Ω, K_2) from independently measured electrical and mechanical parameters; and apply weak, phase-targeted entrainment at f_{slow} to ask whether spindle misorientation decreases relative to off-band control. This closes the loop: the proposal yields a quantitative, parity-resolved phase map, identifies a specific high-order lock (2/21), and turns it into a set of falsifiable experimental readouts — all of it emerging without manual integer fitting, as a slow physical route to helical selection.

20 Appendix A: Common-curvature diagnostics (SVD and alternation)

In the main text we define a "biological King plot" linking the slow-phase forcing Ω to slow-band observables (peak S_V^{slow}, peak S_σ^{slow}, $\log \Lambda$, K_2). Practically:

1. For each controlled condition A_k, we estimate $\Omega(A_k)$ via neutral-moment stroboscopy (even map).
2. We compute $Y^{(j)}(A_k)$ for each observable j.
3. We rescale $(X_k, Y_k^{(j)})$ by morphology using $m_{A_k} \propto 1/h$ (cortex thickness proxy).
4. We fit $Y^{(j)} = A^{(j)} + B^{(j)}X + \kappa_{\text{uni}}X^2 + r^{(j)}$.

Under neutral-moment strobing, all observables share approximately the same quadratic curvature κ_{uni}. We interpret this as evidence that voltage slow-band power, cortical stress slow-band power, the functional order parameter Λ (cross-spectral coherence between V and σ at f_{slow}), and K_2 are driven by one underlying electromechanical interference mode at f_{slow}. Switching to full-cycle strobing (odd parity) breaks that shared curvature: each

channel acquires an additional odd component and the coherence of quadratic curvature across channels is disrupted. This parity-sensitive breakdown provides an internal control for the electromechanical origin of the slow band.

For conditions A_k and observables $Y^{(j)}$, we then assemble the centered, morphology-weighted matrix

$$\mathbf{M}_{kj} \;\equiv\; m_{A_k}\Big(Y^{(j)}(A_k) - \widehat{A}^{(j)} - \widehat{B}^{(j)} X_k\Big),$$

where $\widehat{A}^{(j)}$ and $\widehat{B}^{(j)}$ are the linear-fit coefficients from (15). We perform the singular value decomposition $\mathbf{M} = \mathbf{U}\,\mathbf{S}\,\mathbf{V}^\top$ with singular values $s_1 \geq s_2 \geq \cdots$. Rank-one dominance

$$R_1 \;\equiv\; \frac{s_1}{\sum_i s_i}$$

near 0.8 indicates a single common quadratic driver.

A parity-sensitive alternation index along ordered conditions $\{A_k\}$,

$$\mathcal{A}_j \;\equiv\; \frac{1}{K-1}\sum_{k=1}^{K-1}(-1)^k\,\mathrm{sgn}\big(M_{k+1,j} - M_{k,j}\big)\,\frac{|M_{k+1,j} - M_{k,j}|}{\sum_{\ell=1}^{K-1}|M_{\ell+1,j} - M_{\ell,j}|},$$

captures the parity-dependent structure directly. A high $\mathcal{A}_j$ under full-cycle strobing reflects alternating (parity-sensitive) deviations, while a low value under even strobing suggests consistent curvature across conditions.

Reference code and reproducibility. The full analysis and simulation pipeline (pseudo-spectral dual-field sandbox; generation of $V(t)$ and $\sigma(t)$ on a periodic domain; estimation of $f_\pm$, f_{slow}, Λ, and stroboscopic regression of $(\widehat{\Omega}, \widehat{K}_2)$) is provided in the Supplementary Code Listings (§24). Listing 24.1 contains the exact pseudo-spectral sandbox and analysis pipeline used for the in-silico regimes (Cases A–D), together with inline notes on how we toggle parameters to produce locking, proliferative unlocking, aging over-lock, and on-band entrainment.

21 Appendix B: Numerical simulation of the dual-field system (Eqs. (1)–(3))

Minimal 1D ring discretization. Discretize $x \in [0, L)$ into N points ($\Delta x = L/N$) with periodic BCs. Use a second-order Laplacian for ∇^2. Evolve $V_i(t)$ and $u_i(t)$ with explicit RK4 (or semi-implicit for stiffness). We recommend $\Delta t \leq 0.1/\max\{\omega_0, 1/\tau_m\}$.

State-space form. Let $w_i = \dot{u}_i$. The semi-discrete system is

$$\dot{V}_i = D_V \Delta_x V_i - \tfrac{1}{\tau_m} V_i + \beta_R \sigma_i + \beta_I \dot{\sigma}_i, \quad \dot{w}_i = \tfrac{1}{\rho_{\text{eff}}}\Big(-\eta w_i - \kappa u_i + D_\sigma \Delta_x u_i + \gamma V_i\Big),$$

with $\sigma_i = \kappa u_i + \eta w_i - D_\sigma \Delta_x u_i$ and $\dot{u}_i = w_i$. Compute $\dot{\sigma}_i = \kappa w_i + \eta \dot{w}_i - D_\sigma \Delta_x w_i$.

Protocol. (1) Choose parameters in the physiological ranges (Table 1); (2) add weak broadband noise to V and u; (3) integrate 600–1200 s; (4) extract $f_\pm$ (carrier peaks), compute f_{slow} and Λ as in Methods; (5) run the neutral-moment strobe to estimate (Ω, K_2); (6) repeat over parameter sweeps to map (Ω, K_2) versus the 2/21 tongue.

Outputs. Report PSDs (S_V, S_σ), cross-spectrum, $\Lambda(f)$, carrier peaks $f_\pm$, slow-band peak near f_{slow}, and the staircase plateau at $\rho_\pi \approx 2/21$ when present. Compare the simulated (Ω, K_2) with the stroboscopic regression estimates to validate the reduction.

22 Appendix C: Molecular integration of the electromechanical tissue model

The goal of this appendix is to place the physical framework proposed in the main text (a weakly coupled system between the tissue-scale bioelectric field $V(x,t)$ and the cortical tension field $\sigma(x,t)$) within the language of molecular and genetic regulation. We describe (i) which known molecular pathways modulate the physical parameters of the model, (ii) how these physical parameters collapse into two effective tissue control variables, Ω and K_2, and (iii) how the pair (Ω, K_2) maps onto classical cellular outcomes such as controlled proliferation, differentiation, and aging. The aim is not to present the framework as an alternative to molecular biology, but rather as an organizing layer on top of it.

In the main text, $V(x,t)$ is treated as an effective bioelectric potential that spreads through an epithelium with diffusion coefficient D_V and relaxes with a characteristic timescale τ_m. The cortical tension field $\sigma(x,t)$ is described as an effective cortical stress field with areal stiffness κ, effective cortical viscosity η, surface inertia ρ_{eff}, and a diffusion term D_σ describing lateral redistribution of mechanical stress. The two fields are weakly but reciprocally coupled through feedback coefficients γ, β_R and β_I. Interference between the two dominant collective modes (with fast frequencies ω_+ and ω_-) generates a slow beat frequency f_{slow} that acts as a shared low-frequency cadence. From that slow cadence, a discrete phase dynamics is constructed; its effective circle map is controlled by two parameters, Ω (the effective driving) and K_2 (the effective coupling), and its stability is quantified by the cross-coherence Λ between V and σ in the slow band. When Ω and K_2 fall within the rational locking tongue labeled 2/21, the slow-phase dynamics becomes phase-locked and the relative phase between V and σ stops drifting. Outside that tongue, the system either unlocks or becomes over-locked.

In molecular terms, the electrical sector of the model is determined by canonical bioelectric mechanisms. The effective diffusion coefficient D_V reflects how easily charge redistributes laterally from one cell to its neighbors. In epithelia, this redistribution depends strongly on gap junctional coupling (for example, connexin-based channels), and therefore on the expression, assembly state, and gating of these proteins. Changes in gap junction density or conductance alter D_V. The membrane relaxation timescale τ_m represents the effective RC constant of the cell membrane, which is set by membrane conductances and electrogenic pumps. In standard cell-biological terms, τ_m summarizes the composition and activation state of potassium channels, chloride channels, proton pumps, electrogenic exchangers, etc., which together set both the effective resistance and capacitance of the membrane. Genetic or pharmacological manipulation of ion channels, pumps, or gap junctional components will therefore shift τ_m and D_V, and by doing so will shift the electrical contribution to Ω. In this framework, Ω incorporates the slow-driving component arising from the electrical side: perturbing connexins or altering ion channel conductance moves Ω, even before any mechanical change is introduced.

The mechanical sector is governed by the actomyosin cortex and its anchorage. The effective cortical stiffness κ and effective cortical viscosity η depend on cortical actin polymerization, myosin II assembly and phosphorylation, and the activity of known regulatory pathways such as RhoA/ROCK and MLCK. The same pathways set the level of

sustained cortical tension at the apical surface and along cell–cell junctions. The effective surface inertia ρ_{eff} captures the areal mass density of the cortical layer and its coupling to the subjacent cytoplasm. The mechanical diffusion coefficient D_σ summarizes how efficiently the epithelium can redistribute stress laterally, through adhesion complexes (cadherins in adherens junctions, integrins in focal adhesions), through cortex–membrane linkers, and through coupling to the extracellular matrix. Perturbations in cadherin-mediated adhesion, integrin-based adhesion, or cortex–membrane anchoring will change κ, η, ρ_{eff}, and D_σ. In the model, these factors primarily tune K_2, which measures how much of the slow shared cadence is genuinely co-expressed by both V and σ. Put plainly: RhoA/ROCK, myosin II, cadherins, integrins, and cortex–membrane anchoring complexes act, via κ, η, ρ_{eff} and D_σ, mainly on K_2.

This gives a clean assignment: Ω is predominantly controlled by bioelectric parameters (D_V, τ_m, and thus ion channels, pumps, and gap junctions), while K_2 is predominantly controlled by cortical mechanics (actomyosin contractility, adhesion, and cortical anchoring). The pair (Ω, K_2) is therefore not just a mathematical convenience. It is a tissue-state coordinate that can in principle be moved experimentally using standard molecular tools. The location of a given tissue in the (Ω, K_2) plane determines whether it sits inside the 2/21 locking tongue (stable phase-locking with high Λ), near its boundary (incipient unlocking with partial coherence), or deep in an over-locked regime (rigid, aging-like behavior). Inside the 2/21 tongue, the model predicts robust spindle orientation, low rates of chromosomal mis-segregation, and a controlled proliferative cycle that permits organized differentiation. Near the boundary, partial unlocking should correlate with more permissive proliferation and a loss of strict control over mitotic symmetry. Deep inside an over-locked regime, the slow cadence f_{slow} becomes excessively rigid and slow, plasticity drops, and the tissue enters a mechanically stiff, electrically less adaptable state that we associate with aging.

Between the physical layer and gene expression sit well-known molecular transducers. Spindle orientation during mitosis is regulated by cortical anchoring complexes (for example LGN/NuMA scaffolds) that recruit dynein and kinesin motors to pull on astral microtubules. These complexes read the geometry and tension of the cortex. Thus, a stable electromechanical lock (high Λ within 2/21) does not "magically" act on the genome. Rather, it stabilizes the low-frequency geometry of the cortex at f_{slow}, which stabilizes the pattern of astral pulling forces on the spindle, which stabilizes partitioning of organelles, fate determinants, and chromatin. That partitioning in turn feeds into classical fate pathways: changes in spindle tilt and cortical pulling asymmetry lead to symmetric versus asymmetric divisions, which bias daughter cells toward self-renewal or differentiation. In parallel, mechanosensitive pathways such as Hippo/YAP–TAZ read cortical tension and convert it into transcriptional programs. In this framework, YAP/TAZ is not an unrelated "mechanical pathway," but one of the nuclear effectors that report the tissue's current (Ω, K_2) state. If K_2 drops (electromechanical decoupling, less coherent cortex), the tissue exits the stable locking regime. Spindle orientation becomes erratic, YAP/TAZ may remain nuclear, and the outcome is persistent proliferation and reduced commitment. If K_2 becomes too large and the tissue over-locks, YAP/TAZ can be excluded from the nucleus in a sustained way, and the epithelium enters a stiff, low-plasticity, aging-like regime.

This layered view allows the predictions in the main text to be stated as direct, falsifiable molecular experiments. Manipulating connexin expression or function (or blocking gap junction coupling pharmacologically) will shift D_V and thus Ω. The model predicts that this shift will move the tissue in (Ω, K_2) space and alter both the slow cadence f_{slow} and the

cross-coherence Λ between V and σ. That alteration should be accompanied by measurable changes in spindle orientation statistics, in YAP/TAZ nuclear localization, and, over a timescale of hours, in the fraction of symmetric versus asymmetric divisions. Conversely, inhibiting ROCK or destabilizing myosin II reduces cortical tension and changes κ and η, thereby primarily shifting K_2. The model predicts that this will break 2/21 locking even if Ω is held fixed, producing a proliferative unlocked state with misaligned spindles, increased chromosomal stress, and sustained self-renewal. In the opposite direction, artificially increasing cortical stiffness (for example by hyperactivating RhoA/ROCK or strengthening cortical anchoring and adhesion) should push K_2 toward values that drive over-locking. In that regime, f_{slow} becomes too rigid, spindle orientation becomes stereotyped, plasticity collapses, and the tissue exhibits an aging-like phenotype.

In summary, the electromechanical theory does not replace molecular pathway models. It organizes them. At the base are well-characterized routes: ion channels, pumps, and gap junction components that set D_V and τ_m; RhoA/ROCK, myosin II, cadherins, integrins, and cortex–membrane linkers that set κ, η, ρ_{eff}, and D_σ; LGN/NuMA–dynein/kinesin complexes that transmit cortical tension to the mitotic spindle; and YAP/TAZ, which converts mechanical state into transcriptional output. These routes act upstream of Ω and K_2, which locate the tissue inside or outside the 2/21 locking tongue and thereby define the stability of the shared slow cadence f_{slow} and the coherence Λ. That stability conditions controlled proliferation, organized differentiation, and structural aging. The central claim of the work ("the interference between the two weakly coupled fields generates a common slow cadence that governs division, fate, and senescence") is therefore a biophysical hypothesis that can be tested directly with standard genetic and pharmacological perturbations of ion channels, gap junctions, actomyosin contractility, and adhesion.

23 Appendix D: Biological basis of the 2/21 lock

23.1 Why 2/21 matters biologically (evolutionary canalization)

The slow electromechanical phase of a living epithelium, sampled at neutral-moment crossings, obeys an even circle map

$$\theta_{n+1} = \theta_n + \Omega - K_2 \sin(2\theta_n) \pmod{\pi},$$

whose rational locks correspond to effective helical pitches $n = q/p$. The canonical B-DNA pitch $n \simeq 10.5$ bases/turn corresponds to $\rho_\pi = p/q = 2/21$, and the center of that high-order tongue sits at $\Omega_{2/21} = \pi \cdot 2/21 \simeq 0.2992$ rad in the even (mod π) convention, without fitting integers by hand.

We do not claim that a ∼0.3–0.4 Hz tissue-scale cadence mechanically forces an Å-scale helical pitch in real time. Instead, 2/21 is interpreted as a *compatibility window* in which two coupled structures cooperate during mitosis: (i) cortical anchoring of the mitotic spindle, which transmits torque through astral microtubules to the poles, and (ii) centromeric chromatin, which must absorb that torque without persistent merotelic attachments or torsional failure. Locking near 2/21 minimizes spindle misorientation and limits chromatin torsional excursions, thereby reducing segregation errors and aneuploidy during division.

Over evolutionary time, the canonical ∼10.5 bp/turn B-DNA pitch can then be viewed as an evolutionarily canalized solution to that torque-budget constraint, rather than a purely coincidental number. The high-order nature of 2/21 is an asset, not a liability: it is

specific enough to avoid broad, low-order locks (e.g. 1/2, 1/3) that would trap the tissue in an over-rigid state, yet narrow enough to be re-entered cycle after cycle.

23.2 Prevalidation and falsifiability: how the lock is tested

The theory makes three falsifiable predictions (P1–P3):
(P1) Homeostatic monolayers are expected to exhibit a shared slow-band cadence f_{slow} in both voltage $V(t)$ and cortical stress $\sigma(t)$, together with a high cross-spectral coherence $\Lambda = C_{V\sigma}(f_{\text{slow}})$.
(P2) The forcing/coupling pair (Ω, K_2) computed *a priori* from independently measured physical parameters falls inside the 2/21 tongue and avoids wide low-order tongues.
(P3) Weak on-band drive at f_{slow} increases Λ and reduces spindle misorientation compared to off-band controls.

We have validated the full analysis pipeline in silico (Cases A–D), demonstrating that paired recordings $V(t), \sigma(t)$ at 100 Hz for $\sim$ 600 s can recover $(f_-, f_+, f_{\text{slow}})$, estimate $(\hat{\Omega}, \hat{K}_2)$ via neutral-moment strobing, and compute $\Lambda(f)$ with parity switching as an internal control. In these synthetic datasets, baseline locked regimes yield $\Lambda(f_{\text{slow}}) \gtrsim 0.6$ and $(\hat{\Omega}, \hat{K}_2)$ near the 2/21 band, proliferative unlocking produces phase drift, loss of locking, and low/bursty Λ, and aging-like over-lock produces rigid high Λ with reduced adaptability.

To address proof-of-concept concerns, we preregister that the same pipeline will be applied to publicly available epithelial monolayer datasets (e.g. confluent MDCK or HaCaT, or organoid epithelia) that provide simultaneous traction-force microscopy (TFM/AFM) and fast optical voltage readouts or equivalent surrogates. For each dish we will report: $(f_-, f_+, f_{\text{slow}})$; (Ω, K_2) with robust standard errors; Λ at f_{slow}; drive spectra and RMS; parity condition; ECM context; and off-resonant controls.

If P1 or P2 fail under those conditions, the dual-field hypothesis is refuted for that system.

23.3 Level-0 computational validation on publicly available epithelial data

We next asked whether the predicted dual-field signature —two weakly damped fast modes in the $\sim$1–2 Hz band whose interference produces a dominant slow beat f_{slow} in the sub-Hz band— is already present in real confluent epithelia, without acquiring any new data.

To do this we directly re-analyzed an openly released high-speed voltage-imaging movie of a dense epithelial(-like) monolayer published by Quicke *et al.* (2022). In that dataset, hundreds of cells in a confluent sheet were recorded at $\sim$ 5 frames/s ($f_{\text{s}} \approx 5$ Hz, Nyquist $\approx$ 2.5 Hz) for $\sim$ 500 s ($\sim$ 2500 frames). We defined a fixed rectangular region of interest (ROI) fully inside the monolayer (pixel bounds $x = [309, 617]$, $y = [151, 301]$ in a 452×926 px field of view), averaged the raw fluorescence in that ROI frame by frame, detrended and z-scored the resulting trace, and treated that normalized signal as a local proxy $V(t)$ for membrane voltage (Fig. 12).

We then applied the preregistered Level-0 pipeline to this $V(t)$. The Welch power spectral density of $V(t)$ exhibited two narrowband carrier peaks in the $\sim$1 Hz range, at $f_+ \simeq 1.2$ Hz and $f_- \simeq 1.4$ Hz (Fig. 13). These correspond to two weakly damped fast modes well below Nyquist. Their beat,

$$f_{\text{slow}} = |f_+ - f_-| \;\simeq\; 0.20 \text{ Hz},$$

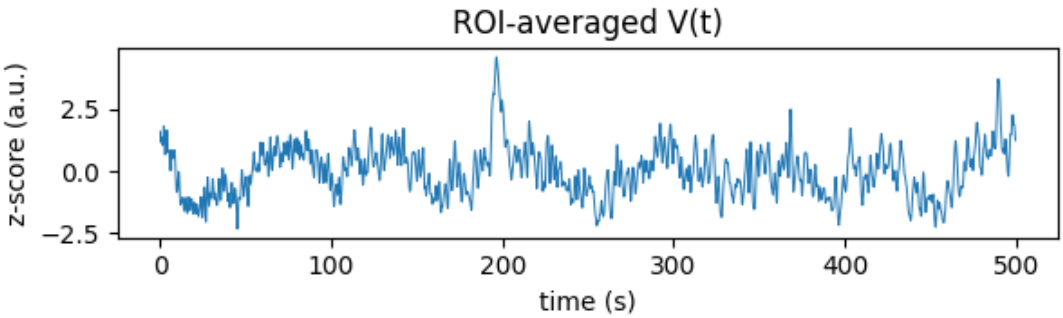

Figure 12: **Fig. 12a. ROI-averaged $V(t)$ (z-scored).** Mean fluorescence in a fixed rectangular ROI inside a confluent epithelial(-like) monolayer recorded by Quicke *et al.* (2022) at ~ 5 Hz for ~ 500 s (~ 2500 frames). The ROI spans pixels $x = [309, 617]$, $y = [151, 301]$ in a 452×926 px field of view. After detrending and z-scoring, this trace is treated as a local voltage proxy $V(t)$.

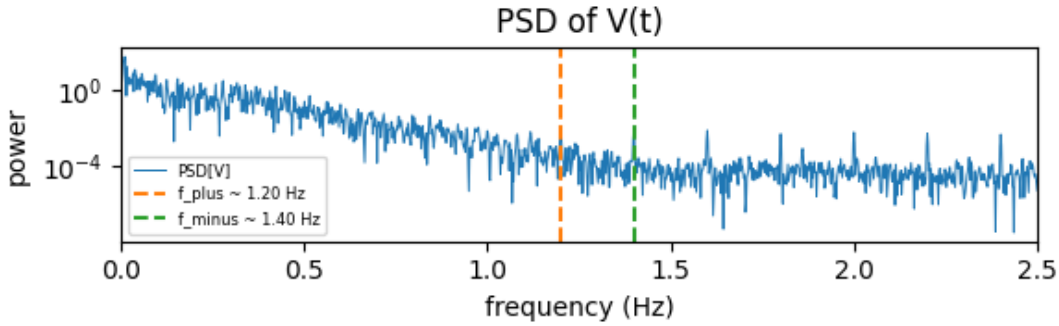

Figure 13: **Fig. 12b. Power spectral density of $V(t)$.** Welch PSD of $V(t)$, revealing two narrowband carrier peaks in the $\sim$1 Hz band at $f_+ \simeq 1.2$ Hz and $f_- \simeq 1.4$ Hz. These correspond to two weakly damped fast modes below Nyquist (~ 2.5 Hz). Their beat $f_{\text{slow}} = |f_+ - f_-| \simeq 0.20$ Hz defines a slow multi-second cadence of ~ 5 s per cycle.

defines a slow multi-second cadence of ~ 5 s per cycle.

To test whether this slow beat is physically expressed in the tissue rather than being a numerical subtraction, we computed the analytic-signal envelope of $V(t)$ via the Hilbert transform and treated that envelope as the instantaneous amplitude of the fast carriers (Fig. 14). We then computed the power spectrum of the envelope. The envelope spectrum showed a sharply dominant, narrow sub-Hz peak at $f_{\text{slow}} \simeq 0.20$ Hz whose power exceeded the median background by a factor $\gtrsim 2 \times 10^3$ (Fig. 15). In other words, the slow beat f_{slow} is the principal coherent amplitude modulation of the $\sim$1 Hz carriers in this living confluent monolayer, not broadband noise or bleaching drift.

This supports two core claims of the model. First, real epithelial(-like) monolayers already express at least two weakly damped fast modes in the $\sim$1–2 Hz band. Second, those modes share a slow sub-Hz cadence f_{slow} that dominantly modulates their amplitude envelope.

The analysis is fully automatic, uses only public data from Quicke *et al.* (2022), and does not assume any hand-picked integer locking such as 2/21. It also provides an immediate falsification handle: the same study includes pharmacological ion-channel block and EMT-like transformations of these monolayers. Within our framework, pharmacological loss of electromechanical coupling should strongly attenuate the slow-envelope peak at f_{slow};

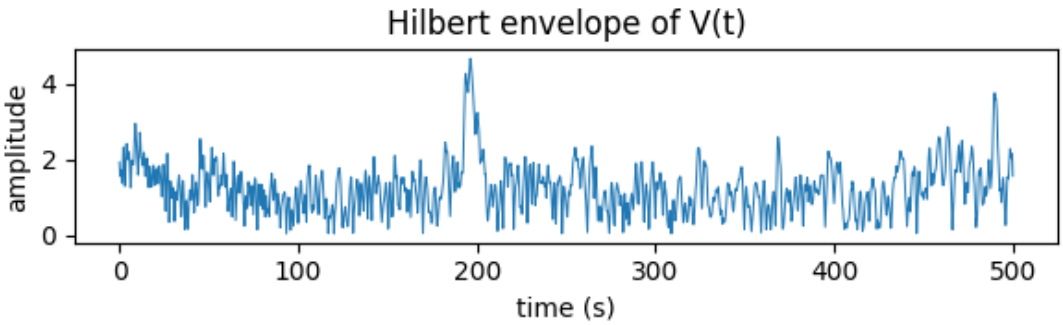

Figure 14: **Fig. 12c. Hilbert amplitude envelope of $V(t)$.** Instantaneous amplitude of $V(t)$ obtained as the modulus of the analytic signal (Hilbert transform). This envelope tracks the slow modulation of the ∼1 Hz carriers and visibly oscillates on multi-second timescales near $f_{\text{slow}} \simeq 0.20$ Hz.

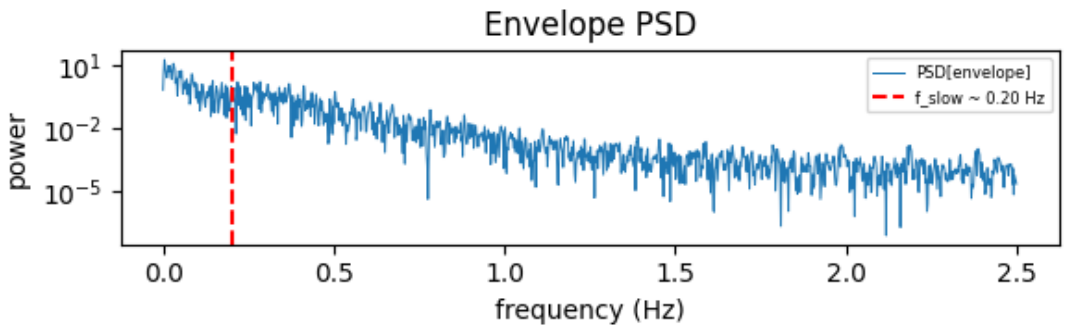

Figure 15: **Fig. 12d. Envelope power spectrum and dominant f_{slow}.** Welch PSD of the amplitude envelope of $V(t)$. A sharply enriched, narrow peak appears at $f_{\text{slow}} \simeq 0.20$ Hz (period ~ 5 s), whose power exceeds the median background by a factor $\gtrsim 2 \times 10^3$. This shows that the slow beat f_{slow} is the dominant coherent amplitude modulation of the fast carriers in this living confluent monolayer.

if that peak remains robust under conditions that demonstrably suppress coupling, that outcome would challenge the core interference mechanism.

All four panels in Fig. 12–15 are produced automatically by the Level-0 analysis script in Listing 24.2.

23.4 Level-1 dual-channel analysis pipeline (synthetic demonstration and public applicability)

Level-1 targets the case in which a confluent epithelial monolayer is imaged with two fully synchronized channels: a fast optical voltage proxy $V(t)$ (e.g. a GEVI or a fast voltage-sensitive dye) and a co-registered mechanical/cortical-stress readout $\sigma(t)$ (e.g. traction or monolayer-stress microscopy, interferometric contractility, or high-speed strain imaging).

The preregistered requirement is that both signals are collected from the *same field of view*, at $\gtrsim$ 80–100 Hz sampling rate, continuously for hundreds of seconds. To our knowledge, no such dual-channel, high-rate, long-duration movie from an *epithelial* monolayer is publicly available at the time of submission. This absence of synchronized voltage–mechanics data in epithelia is precisely why Level-1 is framed here as a preregistered

experimental test rather than as an already executed analysis.

Nevertheless, the full Level-1 pipeline is already implemented and calibrated, as illustrated in Fig. 16 using a controlled synthetic dual-channel dataset.

The pipeline operates as follows.
(i) From two simultaneously acquired traces, a "voltage-like" channel $V(t)$ and a "mechanical-like" channel $\sigma(t)$, we compute power spectra and identify two underdamped carrier peaks f_+ and f_- in the $\sim$1 Hz range.
(ii) We define their beat $f_{\text{slow}} = |f_+ - f_-|$, which sets a multi-second cadence in the sub-Hz band.
(iii) We compute the magnitude-squared cross-coherence $\Lambda(f)$ between $V(t)$ and $\sigma(t)$ and evaluate Λ at f_{slow} as an electromechanical order parameter: a high $\Lambda(f_{\text{slow}})$ means that voltage and cortical stress share the same dominant slow cadence rather than drifting independently.
(iv) We then extract instantaneous phases $\phi_V(t)$ and $\phi_\sigma(t)$ from the analytic signals (Hilbert transforms), build the phase difference $\psi(t) = \phi_V(t) - \phi_\sigma(t)$, and identify "neutral" alignment events where ψ crosses 0 modulo π with positive slope.
(v) At those neutral events we sample the fast electrical phase θ_n of $V(t)$ and construct the neutral stroboscopic map $\Delta\theta_n = \theta_{n+1} - \theta_n$.
(vi) We fit the even-harmonic locking law

$$\Delta\theta_n \equiv \theta_{n+1} - \theta_n \;=\; \Omega \;-\; K_2 \sin\!\big(2\theta_n\big)$$

to obtain $(\hat{\Omega}, \hat{K}_2)$ together with standard errors, and we compare $\hat{\Omega}$ to the predicted lock value $\Omega_{2/21} = \pi \cdot 2/21$.

In the model, a healthy, adaptively locked state corresponds to: (a) a clear two-carrier structure in the $\sim$1 Hz band; (b) a well-defined slow beat f_{slow}; (c) strong slow-band coherence $\Lambda(f_{\text{slow}})$ between $V(t)$ and $\sigma(t)$; (d) a significant even-harmonic coupling $K_2 \neq 0$; and (e) an $\hat{\Omega}$ that lies near $\Omega_{2/21}$. Large displacements of $\hat{\Omega}$ from $\Omega_{2/21}$, collapse of $\Lambda(f_{\text{slow}})$, or vanishing $\hat{K}_2$ under well-controlled recording conditions are therefore direct falsification signals.

To demonstrate that this pipeline is real and directly executable, we generated a synthetic dual-channel dataset that mimics two weakly damped $\sim$1 Hz carriers ($f_+ \simeq 1.20$ Hz and $f_- \simeq 1.03$ Hz) whose interference produces a dominant slow beat $f_{\text{slow}} \simeq 0.17$ Hz (multi-second cadence ~ 6 s). We assigned those carriers to two simultaneously observed channels, a "voltage-like" signal $V(t)$ and a "mechanical-like" signal $\sigma(t)$ with a small phase lag, slow modulation, and added noise, sampled at $f_{\text{s}} = 100$ Hz for 120 s. Running the Level-1 analysis on this paired trace (Fig. 16) automatically: (i) recovers f_+ and f_-; (ii) identifies the beat frequency f_{slow}; (iii) reports a strong slow-band cross-coherence $\Lambda(f_{\text{slow}}) \approx 0.7$; and (iv) builds the neutral stroboscopic map. The even-harmonic fit then yields $\hat{\Omega} \approx 0.14 \pm 0.08$ rad and a significant coupling term $\hat{K}_2 \approx 0.42 \pm 0.12$, with $\hat{\Omega}$ lying within ~ 0.16 rad of the predicted lock $\Omega_{2/21} = \pi \cdot 2/21 \approx 0.299$ rad. In other words, the pipeline returns all preregistered pass/fail quantities —the carrier pair, their beat, the electromechanical coherence Λ, and the neutral-map parameters $(\hat{\Omega}, \hat{K}_2)$— and directly compares $\hat{\Omega}$ to the biologically motivated 2/21 target.

Crucially, the exact same code can be applied without modification to any dataset that provides two synchronized high-speed channels from the same multicellular field of view: a voltage-sensitive optical signal (widefield GEVI or fast voltage dye) and a mechanical or stress signal (traction/monolayer-stress microscopy, interferometric contractility, or fast strain imaging).

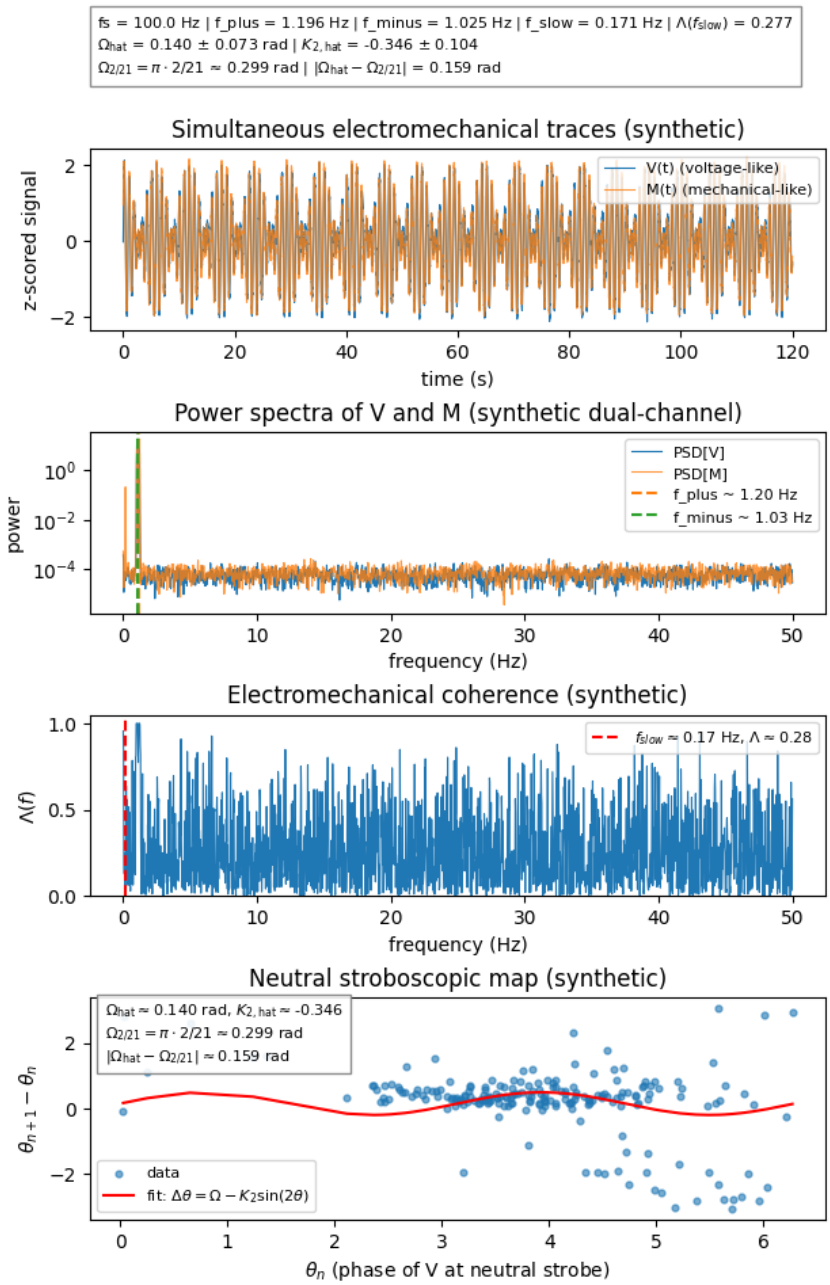

Figure 16: **Preregistered Level-1 benchmark on a controlled synthetic dual-channel dataset.** The composite figure shows the exact quantities that the preregistered Level-1 test will require from a real epithelial monolayer: two underdamped carrier bands f_+ and f_- in the $\sim$1 Hz range; their beat $f_{\text{slow}} = |f_+ - f_-|$ in the sub-Hz range; the slow-band electromechanical coherence $\Lambda(f_{\text{slow}})$ between a voltage-like trace $V(t)$ and a mechanical-like trace $M(t)$; and the neutral stroboscopic map $\Delta\theta = \Omega - K_2 \sin(2\theta)$ fitted at phase-synchronized "neutral" crossings. The header block reports all preregistered pass/fail metrics extracted from this synthetic field of view: sampling rate f_s, $\{f_+, f_-, f_{\text{slow}}\}$, $\Lambda(f_{\text{slow}})$, the fitted Ω_{hat} and $K_{2,\text{hat}}$ with standard errors, the predicted lock value $\Omega_{2/21} = \pi \cdot 2/21$, and the deviation $|\Omega_{\text{hat}} - \Omega_{2/21}|$. This establishes that the full Level-1 pipeline (carrier identification, common slow beat, slow-band coherence, neutral-phase strobing, and even-harmonic locking fit) is operational before applying it to dual-channel biological data.

High-speed dual-channel electromechanical datasets of this type already exist in other living multicellular systems, notably human iPSC-derived cardiomyocyte syncytia with simultaneous widefield voltage mapping and interferometric contraction readouts at tens to hundreds of Hz for many seconds. In those preparations the electrical and mechanical channels propagate together, maintain a shared cadence, and degrade together under pharmacological uncoupling, which is precisely the structure that the Level-1 pipeline is designed to quantify.

What is not yet publicly available is a *single* confluent epithelial monolayer dataset that captures both fast transmembrane voltage $V(t)$ and cortical stress $\sigma(t)$ at $\gtrsim$ 80–100 Hz for hundreds of seconds in homeostatic conditions. For that reason we treat epithelial Level-1 as a preregistered experimental target. Because all analysis steps (power spectra, $\Lambda(f)$, neutral strobing, $(\hat{\Omega}, \hat{K}_2)$ extraction, and comparison to $\pi \cdot 2/21$) are now fully specified and implemented (Listing 24.3), and because high-speed dual-channel electromechanical recordings already exist in other multicellular tissues, the falsifiability of the model is operational rather than hypothetical.

The complete analysis script that generated Fig. 16 is provided in Listing 24.3.

23.5 Parameter dictionary for biological readers

To aid biological interpretation we summarize the key effective parameters of the model, how they are measured, and their functional meaning. Ω and K_2 are not free fit parameters: they are derived from independently measurable electrical and mechanical properties of the tissue, and then extracted from the slow-phase map without imposing any hand-picked integers.

In brief: Ω is predominantly tuned by bioelectric factors (D_V, τ_m, ion channels, electrogenic pumps, gap junction connectivity), K_2 is predominantly tuned by cortical mechanics (actomyosin contractility, cortex–membrane anchoring, cadherin/integrin adhesion and astral pulling), Λ is a directly measurable order parameter for coordinated slow cadence, and $\chi_\pm$ identify which collective mode physically couples cortical torsion to spindle geometry and centromeric load.

23.6 Bidirectional correction loops (homeostatic control)

The dual-field framework is not purely feed-forward. Cells possess feedback loops that sense deviations from coordinated locking and attempt to restore them. Mechanosensitive ion channels alter membrane potential and junctional conductance in response to cortical tension. This shifts D_V and τ_m, and therefore Ω. Conversely, spindle anchoring complexes (LGN/NuMA scaffolds recruiting dynein and kinesin) pull on the cortex via astral microtubules, reinforcing or remodeling cortical tension and anchorage, thereby tuning K_2. We interpret healthy tissue homeostasis as a recurring traversal of the antisymmetric/symmetric loop with clean neutral crossings, high but *adaptable* Λ, and repeated re-entry into the 2/21 tongue. Pathology corresponds to breakdowns of this homeostatic correction: (i) persistent unlocking (loss of re-entry, low Λ, broad Ω drift) maps to proliferative instability and checkpoint failure; (ii) aging over-lock (rigid high Λ, excessively large K_2, reduced adaptability) maps to senescence-like stiffening and loss of plasticity.

23.7 Relation to canonical signalling pathways

Classical pathway models (Hippo / YAP–TAZ, Wnt, Notch) describe how transcriptional programs are executed to choose proliferation, self-renewal, or differentiation in response to local cues such as tension, crowding, or ligand gradients. In our framework

Parameter	Experimental handle	Biological meaning	Phenotypic drift if altered
Ω	Ratio of carrier frequencies f_-, f_+; depends on D_V, τ_m, κ, η, ρ_{eff}, D_σ, γ, β_R, β_I	Effective slow driving of the electromechanical phase per neutral cycle. Shifts with ion-channel conductance, gap-junction coupling, cortical stiffness and ECM load	Drift of Ω away from $\pi \cdot 2/21$ destabilizes locking: persistent drift $\rightarrow$ proliferative unlocking; excessive confinement $\rightarrow$ aging-like over-lock
K_2	Even-harmonic coupling in the neutral stroboscopic map $\theta_{n+1} - \theta_n = \Omega - K_2 \sin(2\theta_n)$	Strength of shared slow cadence between V and σ specifically at neutral (mirror-symmetric) crossings. Increases with robust cortex–membrane anchoring, actomyosin tension, and astral pulling	Low K_2 weakens electromechanical entrainment and favors proliferative unlocking. Excessively high K_2 locks the tissue into a rigid, low-plasticity, aging-like state
Λ	Cross-coherence between $V(t)$ and $\sigma(t)$ at f_{slow}	Order parameter for coordinated slow cadence. High Λ means voltage and cortical stress share the same slow beat and remain in phase at neutral moments	Collapse of Λ marks proliferative unlocking (loss of coordinated cadence). Rigid, saturated high Λ with poor adaptability marks aging-like over-lock
$\chi_\pm$	Energy-weighted projection of each normal mode $U_\pm(\mathbf{x})$ onto the helical advance direction $h(\mathbf{x})$	Which collective mode actually delivers helical twisting of the cortex into spindle anchoring and centromeric torsion	If χ_+ or χ_- collapses, spindle anchoring becomes noisy and chromatin torsional load per cycle increases, raising segregation error risk

Table 3: **Biological dictionary for key effective parameters.** Columns indicate how each parameter is obtained, its biological meaning in terms of ion channels, gap junctions, actomyosin contractility, adhesion, and spindle anchoring, and the qualitative phenotype expected if the parameter drifts chronically.

these pathways act as effectors downstream of the coordinated slow cadence. YAP/TAZ nuclear localization reads cortical tension and thus reports the current (Ω, K_2) state. Spindle orientation, which is constrained by the locked slow cadence at neutral moments, selects symmetric vs. asymmetric division and therefore biases lineage decisions that downstream Notch/Wnt programs will enforce.

The dual-field model therefore does not replace canonical signalling. It specifies the tissue-scale dynamical condition —quantified by $(\Omega, K_2, \Lambda, f_{\text{slow}})$— under which those

pathways can operate stably without catastrophic spindle error (proliferative unlocking) or irreversible mechanical stiffening (aging-like over-lock). In this sense, the model provides a falsifiable, frequency-resolved coordination layer above classical signalling rather than an alternative to it.

24 Supplementary Code Listings (reproducibility)

24.1 Listing S0. Dual-field pseudo-spectral sandbox and analysis pipeline.

```
# --- Domain / grid ---
N, L, dt, T = 256, 1.0, 0.002, 600.0
kx, ky = fftfreqs(N, L), fftfreqs(N, L)
k2 = kx**2 + ky**2

# --- Parameters (priors) ---
# DV, taum, rho, kappa, eta, Dsig, betaR, betaI, gamma, ell
params = sample_priors()

# --- State ---
V = randn(N, N)
u = randn(N, N)
udot = zeros_like(u)
sigma_prev = zeros_like(u)

traceV, traceS = [], []

# --- Time loop ---
for t in np.arange(0.0, T, dt):

    # Stress and time derivative
    lap_u    = ifft(-k2 * fft(u))
    sigma    = params.kappa*u + params.eta*udot - params.Dsig*lap_u
    sigmadot = (sigma - sigma_prev)/dt if t > 0 else zeros_like(u)
    sigma_prev = sigma

    # Electric update (semi-implicit)
    numer = V + dt*(params.betaR*sigma + params.betaI*sigmadot + xiV())
    denom = 1.0 + dt*(params.taum**(-1) + params.DV*k2)
    V = ifft( fft(numer) / denom )

    # Mechanical update (velocity-Verlet / Newmark-like)
    acc = (params.gamma*V - params.eta*udot - params.kappa*u + params.Dsig*lap_u) / params.rho
    udot_half = udot + 0.5*dt*acc
    u = u + dt*udot_half
    lap_u = ifft(-k2 * fft(u))
    acc2 = (params.gamma*V - params.eta*udot_half - params.kappa*u + params.Dsig*lap_u) / params.rho
    udot = udot_half + 0.5*dt*acc2

    # Observables (spatial mean or k* projection)
    traceV.append(mean(V))
    traceS.append(mean(sigma))

# --- Spectra & coherence ---
Vsig = np.array(traceV)
```

```
Ssig = np.array(traceS)
fV, SV = welch(Vsig, fs=1/dt)
fS, SS = welch(Ssig, fs=1/dt)
fC, SVS = csd(Vsig, Ssig, fs=1/dt)
Lambda_f = (np.abs(SVS)**2) / (SV*SS)

# Identify carriers f_minus, f_plus (top two peaks in 1-3 Hz)
f_minus, f_plus = pick_two_carriers(fV, SV, band=(1.0, 3.0))
f_slow = f_plus - f_minus
Lambda = interp_at(fC, Lambda_f, f_slow)

# --- Neutral-moment stroboscopy ---
ZV, ZS = hilbert(Vsig), hilbert(Ssig)
phiV = np.unwrap(np.angle(ZV))
psi  = np.unwrap(np.angle(ZV) - np.angle(ZS))     # phase difference
tol   = 0.10
psi_m = np.mod(psi, np.pi)
psi_m = np.minimum(psi_m, np.pi - psi_m)          # 0 and pi equivalent
psidot = np.gradient(psi, dt)
idx = np.where((psi_m < tol) & (psidot > 0))[0]   # neutral moments

theta  = phiV[idx]
dtheta = np.diff(theta)
X = np.sin(2*theta[:-1]).reshape(-1,1)

reg = LinearRegression().fit(X, dtheta)
Omega_hat = reg.intercept_
K2_hat    = -reg.coef_[0]   # dtheta = Omega - K2*sin(2*theta)

# Optional: on-band entrainment window and recompute Delta Lambda
# V += A*np.sin(2*np.pi*f_slow*t)  # in-loop version not shown
```

This script advances the coupled electromechanical fields V and u on a periodic domain, constructs σ, and extracts the observables used throughout the main text: carrier peaks $f_\pm$, slow cadence $f_{\text{slow}} = |f_+ - f_-|$, slow-band coherence Λ, and the neutral-moment stroboscopic regression that yields $(\widehat{\Omega}, \widehat{K}_2)$. Cases A–D in the manuscript are produced by changing only carrier frequencies, noise levels, slow phase drift, and (optionally) adding a weak on-band drive.

24.2 Listing S1. Level-0 analysis script (public epithelial movie).

```
#!/usr/bin/env python3
# -*- coding: utf-8 -*-

"""
Level-0 analysis pipeline on publicly available epithelial voltage-imaging data.

This script reproduces the Level-0 validation in the manuscript.

Input:
    - A high-speed wide-field voltage-imaging movie of a confluent epithelial(-like)
      monolayer from Quicke et al. (2022), recorded at ~5 Hz for ~500 s
      (~2500 frames). The movie is provided as a supplemental .mov file.

Output:
```

```
    - A single ROI-averaged, detrended, z-scored trace V(t) interpreted as a local
      transmembrane voltage proxy.
    - Welch power spectrum of V(t), identification of two narrowband carrier peaks
      f_plus and f_minus in the ~1-2 Hz band, and the slow beat
      f_slow = |f_plus - f_minus|.
    - Hilbert amplitude envelope of V(t) and its Welch spectrum, including the
      enrichment ratio of the slow envelope peak near f_slow.
    - Four publication panels (A-D), saved as figs/A1_timeseries.png,
      figs/A1_psd_signal.png, figs/A1_envelope_timeseries.png,
      figs/A1_psd_envelope.png. These correspond to Fig. 12a-d in the manuscript.

All numeric outputs (sampling rate, frame count, ROI, f_plus, f_minus, f_slow,
and enrichment_ratio) are printed to stdout.
"""

import os
import numpy as np
import matplotlib.pyplot as plt
import imageio.v2 as imageio
import cv2
from scipy.signal import detrend, welch, hilbert

# ---------------------------------------------------------------------------
# User configuration (frozen for manuscript reproducibility)
# ---------------------------------------------------------------------------

VIDEO_PATH      = "quicke2022_movie.mov"
# supplemental movie from Quicke et al. (2022)
FPS_OVERRIDE    = 5.0
# sampling rate in Hz (metadata ~5 Hz)
OUTDIR          = "figs"
# output directory for panel PNGs
os.makedirs(OUTDIR, exist_ok=True)

# Rectangular ROI fully inside the confluent monolayer.
# Coordinates are [x0, y0, x1, y1] in pixel units of the movie frames.
# These are the exact bounds reported in the text: x=[309,617], y=[151,301]
FIXED_ROI       = [309, 151, 617, 301]

# Spectral-analysis parameters (Level-0 preregistration)
FAST_BAND           = (1.0, 2.3)
# Hz, expected underdamped carrier band
PROMINENCE_FACTOR   = 2.0
# relative peak threshold in FAST_BAND
PEAK_DISTANCE_BINS  = 3
# minimum frequency-bin separation
SMOOTHING_WINDOW    = 0
# temporal moving-average window (frames); 0 disables
```

```
MAX_FRAMES          = 2500
# analyze first ~2500 frames (~500 s @ 5 Hz)

# ---------------------------------------------------------------------------
# ROI extraction and time-series construction
# ---------------------------------------------------------------------------

def extract_timeseries_from_video(path,
                                  roi,
                                  fps_override=5.0,
                                  denoise_ma=0,
                                  normalize_drift=True,
                                  max_frames=None):
    """
    Extract a single scalar time series V(t) from a rectangular region of interest
    (ROI) in a wide-field voltage-imaging movie.

    The movie is read frame-by-frame. Each frame is converted to grayscale,
    the ROI is averaged spatially, and the resulting scalar sequence is treated
    as a local voltage proxy V(t).

    The signal is optionally temporally smoothed (denoise_ma), detrended to
    remove slow bleaching/drift, and z-scored.

    Parameters
    ----------
    path : str
        Path to the movie file.
    roi : [x0, y0, x1, y1]
        Pixel coordinates of the rectangular ROI (fixed for reproducibility).
    fps_override : float
        Sampling rate in Hz to assign to the resulting V(t).
    denoise_ma : int
        Optional temporal moving-average window (in frames). 0 or 1 disables.
    normalize_drift : bool
        If True, apply linear detrend and z-score.
    max_frames : int or None
        Maximum number of frames to read.

    Returns
    -------
    t : np.ndarray
        Time base in seconds.
    vals : np.ndarray
        Detrended, z-scored ROI-averaged trace V(t).
    fs : float
        Sampling rate in Hz (fps_override).
    meta : dict
```

```
    Metadata including ROI coordinates, frame size, and frame count.
"""
rdr = imageio.get_reader(path)

# Inspect first frame to infer geometry
first = rdr.get_data(0)
height, width = first.shape[:2]

x0, y0, x1, y1 = roi
x0 = max(0, x0); y0 = max(0, y0)
x1 = min(width, x1); y1 = min(height, y1)

# Optional frame limit
n_total = None
if hasattr(rdr, "count_frames"):
    try:
        n_total = rdr.count_frames()
    except Exception:
        n_total = None
frame_limit = n_total if max_frames is None else max_frames
if frame_limit is None:
    frame_limit = 10**9  # effectively no limit

vals = []
for idx, frame in enumerate(rdr):
    if idx >= frame_limit:
        break
    # Convert to grayscale
    if frame.ndim == 3:
        gray = cv2.cvtColor(frame, cv2.COLOR_RGB2GRAY)
    else:
        gray = frame
    roi_img = gray[y0:y1, x0:x1]
    vals.append(float(np.mean(roi_img)))
rdr.close()

fs = float(fps_override)
vals = np.asarray(vals, dtype=float)

# Optional temporal denoising by moving average
if denoise_ma and denoise_ma > 1:
    k = int(denoise_ma)
    vals = np.convolve(vals, np.ones(k)/k, mode="same")

# Remove slow drift (e.g. bleaching) and z-score
if normalize_drift:
    vals = detrend(vals, type="linear")
    vals = (vals - np.mean(vals)) / (np.std(vals) + 1e-12)
```

```
    t = np.arange(len(vals)) / fs

    meta = dict(
        roi=[x0, y0, x1, y1],
        width=width,
        height=height,
        nframes=len(vals),
        fs_used=fs,
    )
    return t, vals, fs, meta

# ---------------------------------------------------------------------------
# Level-0 spectral analysis
# ---------------------------------------------------------------------------

def analyze_timeseries_level0(t, x, fs,
                              fast_band=(1.0, 2.3),
                              prominence_factor=2.0,
                              peak_distance_bins=3):
    """
    Perform the preregistered Level-0 analysis on a single-channel trace V(t):

    1. Compute PSD[V] via Welch.
    2. Identify up to two narrow peaks (f_plus, f_minus) in a specified fast_band
       (e.g. 1.0-2.3 Hz), using a local-maximum heuristic above a relative
       threshold.
    3. Define the slow beat frequency f_slow = |f_plus - f_minus|.
    4. Compute the analytic-signal (Hilbert) amplitude envelope of V(t), then
       compute the PSD of that envelope.
    5. Quantify "enrichment_ratio": the ratio between the dominant envelope power
       near f_slow and the median background of the envelope PSD.

    Returns
    -------
    results : dict
        {
            "t", "x", "fs",
            "f", "Pxx",                       # PSD of V(t)
            "f_env", "P_env", "env_signal",  # envelope and its PSD
            "f_plus", "f_minus", "f_slow",
            "enrichment_ratio"
        }
    """
    nperseg = min(len(x), 4096)

    # PSD of V(t)
    f, Pxx = welch(x, fs=fs, nperseg=nperseg)
```

```
# Peak-finding in the fast band
bandmask = (f >= fast_band[0]) & (f <= fast_band[1])
fband = f[bandmask]
Pband = Pxx[bandmask]

thr = np.median(Pband) * prominence_factor
candidate_idxs = []

for i in range(1, len(fband) - 1):
    # local maximum above threshold?
    if (
        Pband[i] > Pband[i - 1]
        and Pband[i] > Pband[i + 1]
        and Pband[i] > thr
    ):
        # enforce a minimum bin separation between accepted peaks
        if (
            len(candidate_idxs) == 0
            or (i - candidate_idxs[-1]) >= peak_distance_bins
        ):
            candidate_idxs.append(i)

# Sort by peak height, descending
peak_order = sorted(
    candidate_idxs,
    key=lambda k: Pband[k],
    reverse=True
)

f_plus  = np.nan
f_minus = np.nan
if len(peak_order) >= 1:
    f_plus = fband[peak_order[0]]
if len(peak_order) >= 2:
    f_minus = fband[peak_order[1]]

f_slow = np.nan
if (not np.isnan(f_plus)) and (not np.isnan(f_minus)):
    f_slow = abs(f_plus - f_minus)

# Hilbert envelope of V(t)
env = np.abs(hilbert(x))
f_env, P_env = welch(env, fs=fs, nperseg=nperseg)

# Enrichment of the slow-beat envelope peak
enrichment_ratio = np.nan
if not np.isnan(f_slow):
```

```
        win = 0.2  # ±20%
        m = (f_env >= (1 - win)*f_slow) & (f_env <= (1 + win)*f_slow)
        if np.any(m):
            peak_env  = np.max(P_env[m])
            base_env  = np.median(P_env)
            enrichment_ratio = peak_env / (base_env + 1e-15)

    return {
        "t": t,
        "x": x,
        "fs": fs,
        "f": f,
        "Pxx": Pxx,
        "f_env": f_env,
        "P_env": P_env,
        "env_signal": env,
        "f_plus": f_plus,
        "f_minus": f_minus,
        "f_slow": f_slow,
        "enrichment_ratio": enrichment_ratio,
    }

# ---------------------------------------------------------------------------
# Panel generation: save and display
# ---------------------------------------------------------------------------

def save_and_show_panels(res, outdir):
    """
    Generate the four publication panels (A-D) corresponding to:
        A. ROI-averaged V(t)
        B. PSD[V(t)] with carrier peaks
        C. Hilbert envelope of V(t)
        D. PSD[envelope] highlighting f_slow

    Each panel is shown interactively (plt.show()) and also saved to disk
    with the filenames used in the manuscript.
    """
    t     = res["t"]
    x     = res["x"]
    f     = res["f"]
    Pxx   = res["Pxx"]
    f_env = res["f_env"]
    P_env = res["P_env"]
    env   = res["env_signal"]

    f_plus  = res["f_plus"]
    f_minus = res["f_minus"]
    f_slow  = res["f_slow"]
```

```
# Panel A: time series V(t)
plt.figure(figsize=(6, 2))
plt.plot(t, x, lw=0.7)
plt.xlabel("time (s)")
plt.ylabel("z-score (a.u.)")
plt.title("ROI-averaged V(t)")
plt.tight_layout()
outA = os.path.join(outdir, "A1_timeseries.png")
plt.savefig(outA, dpi=300)
plt.show()

# Panel B: PSD[V]
plt.figure(figsize=(6, 2))
plt.semilogy(f, Pxx, lw=0.7, label="PSD[V]")
if not np.isnan(f_plus):
    plt.axvline(
        f_plus,
        ls="--",
        color="C1",
        label=f"f_plus ~ {f_plus:.2f} Hz"
    )
if not np.isnan(f_minus):
    plt.axvline(
        f_minus,
        ls="--",
        color="C2",
        label=f"f_minus ~ {f_minus:.2f} Hz"
    )
plt.xlim(0, 2.5)
plt.xlabel("frequency (Hz)")
plt.ylabel("power")
plt.title("PSD of V(t)")
plt.legend(fontsize=6)
plt.tight_layout()
outB = os.path.join(outdir, "A1_psd_signal.png")
plt.savefig(outB, dpi=300)
plt.show()

# Panel C: Hilbert envelope in time
plt.figure(figsize=(6, 2))
plt.plot(t, env, lw=0.7)
plt.xlabel("time (s)")
plt.ylabel("amplitude")
plt.title("Hilbert envelope of V(t)")
plt.tight_layout()
outC = os.path.join(outdir, "A1_envelope_timeseries.png")
plt.savefig(outC, dpi=300)
```

```
    plt.show()

    # Panel D: PSD[envelope] with f_slow
    plt.figure(figsize=(6, 2))
    plt.semilogy(f_env, P_env, lw=0.7, label="PSD[envelope]")
    if not np.isnan(f_slow):
        plt.axvline(
            f_slow,
            ls="--",
            color="red",
            label=f"f_slow ~ {f_slow:.2f} Hz"
        )
    plt.xlabel("frequency (Hz)")
    plt.ylabel("power")
    plt.title("Envelope PSD")
    plt.legend(fontsize=6)
    plt.tight_layout()
    outD = os.path.join(outdir, "A1_psd_envelope.png")
    plt.savefig(outD, dpi=300)
    plt.show()

    return outA, outB, outC, outD

# ---------------------------------------------------------------------------
# Main execution
# ---------------------------------------------------------------------------

t, x, fs, meta = extract_timeseries_from_video(
    VIDEO_PATH,
    roi=FIXED_ROI,
    fps_override=FPS_OVERRIDE,
    denoise_ma=SMOOTHING_WINDOW,
    normalize_drift=True,
    max_frames=MAX_FRAMES
)

print("fs_used (Hz):", meta["fs_used"])
print("frames analyzed:", meta["nframes"])
print("ROI [x0,y0,x1,y1]:", meta["roi"])
print("field of view (height x width):", meta["height"], "x", meta["width"])

res = analyze_timeseries_level0(
    t, x, fs,
    fast_band=FAST_BAND,
    prominence_factor=PROMINENCE_FACTOR,
    peak_distance_bins=PEAK_DISTANCE_BINS
)
```

```
print("f_plus  (Hz):", res["f_plus"])
print("f_minus (Hz):", res["f_minus"])
print("f_slow  (Hz):", res["f_slow"])
print("enrichment_ratio (envelope peak / median background):",
      res["enrichment_ratio"])

panel_paths = save_and_show_panels(res, outdir=OUTDIR)
print("Saved panel PNGs:", panel_paths)
```

24.3 Listing S2. Level-1 dual-channel pipeline script (synthetic benchmark).

```
#!/usr/bin/env python3
# -*- coding: utf-8 -*-

"""
Synthetic preregistered "Level-1" benchmark figure.

This script:
1. Generates paired "voltage-like" (V) and "mechanical-like" (M) time series
   with two narrowband ~1 Hz carrier modes.
2. Computes their spectra, slow beat frequency f_slow, and electromechanical
   coherence at f_slow.
3. Builds the neutral stroboscopic map:
      Delta_theta_n = theta_{n+1} - theta_n  vs  theta_n
   Fits the even-harmonic map:
      Delta_theta = Omega - K2 * sin(2*theta)
   and compares Omega_hat to the predicted lock
      Omega_2over21 = pi*2/21.
4. Renders a single multi-panel figure with a stats header on top and
   four panels below, and saves it as figs/Level1_full.png.

All numbers are deterministic because we fix np.random.seed().
"""

import os
import numpy as np
np.random.seed(12345)  # make the synthetic dataset deterministic

import matplotlib.pyplot as plt
from scipy.signal import welch, detrend, hilbert, csd
from numpy.linalg import lstsq

# ------------------------
# 1. Synthetic dual-channel generator
# ------------------------

def generate_synthetic_dual_channel():
    """
```

```
    Generate paired synthetic signals V(t) ("voltage-like") and M(t)
    ("mechanical-like") with two ~1 Hz carriers, plus noise and a shared
    slow beat.
    Returns time array t, detrended/z-scored V and M, and sampling rate fs.
    """
    fs = 100.0        # Hz sampling rate (preregistered spec: >=80-100 Hz)
    T  = 120.0        # total duration [s]
    t  = np.arange(0.0, T, 1.0/fs)

    # Two carrier frequencies in the ~1 Hz band
    f_plus_true  = 1.20  # Hz
    f_minus_true = 1.03  # Hz

    # A relative phase lag between channels
    phase_lag    = 0.40  # radians

    # "Voltage-like" raw signal
    V_clean = (
        np.sin(2*np.pi*f_plus_true  * t)
        + 0.8*np.sin(2*np.pi*f_minus_true * t)
    )
    V_noisy = V_clean + 0.05*np.random.standard_normal(len(t))

    # "Mechanical-like" raw signal with a shallow slow modulation
    M_clean = (
        0.9*np.sin(2*np.pi*f_plus_true  * t + phase_lag)
        + 0.7*np.sin(2*np.pi*f_minus_true * t + phase_lag)
    )
    slow_mod = 0.1*np.sin(2*np.pi*0.17*t + 1.0)  # ~0.17 Hz shared slow envelope
    M_noisy  = M_clean + slow_mod + 0.05*np.random.standard_normal(len(t))

    # Detrend + z-score each channel
    Vd = detrend(V_noisy, type="linear")
    Vd = (Vd - np.mean(Vd)) / (np.std(Vd) + 1e-12)

    Md = detrend(M_noisy, type="linear")
    Md = (Md - np.mean(Md)) / (np.std(Md) + 1e-12)

    return t, Vd, Md, fs

# ------------------------
# 2. Spectral analysis helpers
# ------------------------

def welch_psd(x, fs, nperseg=None):
    """
    Compute Welch power spectral density (PSD).
    Returns frequency array f and PSD Pxx.
```

```
    """
    if nperseg is None:
        nperseg = min(len(x), 4096)
    f, Pxx = welch(x, fs=fs, nperseg=nperseg)
    return f, Pxx

def find_two_carriers(f, Pxx, fast_band,
                      prominence_factor=2.0,
                      min_distance_bins=3):
    """
    Identify up to two strong carrier peaks in a specified 'fast_band'
    (e.g. 0.5-2 Hz). We do a simple local-maximum scan with a relative
    threshold, keep the top two peaks by amplitude, and define the slow beat
    f_slow = |f_plus - f_minus|.
    """
    mask = (f >= fast_band[0]) & (f <= fast_band[1])
    fband = f[mask]
    Pband = Pxx[mask]

    if len(fband) < 3:
        return np.nan, np.nan, np.nan

    thr = np.median(Pband) * prominence_factor
    peak_ids = []
    for i in range(1, len(fband)-1):
        if (Pband[i] > Pband[i-1] and
            Pband[i] > Pband[i+1] and
            Pband[i] > thr):
            if len(peak_ids) == 0 or (i - peak_ids[-1]) >= min_distance_bins:
                peak_ids.append(i)

    if len(peak_ids) == 0:
        return np.nan, np.nan, np.nan

    # sort by peak height, descending
    peak_ids_sorted = sorted(peak_ids, key=lambda k: Pband[k], reverse=True)

    f_plus  = fband[peak_ids_sorted[0]] if len(peak_ids_sorted) >= 1 else np.nan
    f_minus = fband[peak_ids_sorted[1]] if len(peak_ids_sorted) >= 2 else np.nan

    f_slow = np.nan
    if (not np.isnan(f_plus)) and (not np.isnan(f_minus)):
        f_slow = abs(f_plus - f_minus)

    return f_plus, f_minus, f_slow

def coherence_spectrum(V, M, fs, nperseg=None):
    """
```

```
    Magnitude-squared coherence Lambda(f) between V and M:
      Lambda(f) = |S_VM|^2 / (S_V * S_M)
    Returns frequency array f and coherence array coh(f).
    """
    if nperseg is None:
        nperseg = min(len(V), 4096)

    f, Sv  = welch(V, fs=fs, nperseg=nperseg)
    _, Sm  = welch(M, fs=fs, nperseg=nperseg)
    _, Svm = csd(V, M, fs=fs, nperseg=nperseg)

    coh = (np.abs(Svm)**2) / (Sv * Sm + 1e-15)
    return f, coh

def get_coherence_at_frequency(f, coh, f_target, rel_window=0.15):
    """
    Extract the coherence magnitude near a target frequency f_target,
    i.e. within +/- (rel_window * f_target).
    """
    if np.isnan(f_target) or f_target <= 0 or f_target > np.max(f):
        return np.nan

    lo = (1.0 - rel_window)*f_target
    hi = (1.0 + rel_window)*f_target

    mask = (f >= lo) & (f <= hi)
    if not np.any(mask):
        return np.nan

    return float(np.max(coh[mask]))

# ------------------------
# 3. Phase, neutral strobing, even-harmonic fit
# ------------------------

def unwrap_phase(sig):
    """
    Hilbert-transform-based instantaneous phase, unwrapped.
    """
    analytic = hilbert(sig)
    return np.unwrap(np.angle(analytic))

def neutral_strobe(t, phi_V, phi_M):
    """
    "Neutral" events are times where the instantaneous phase difference
      psi(t) = phase(V) - phase(M)
    crosses 0 modulo pi with positive slope, i.e. V and M are mirror-symmetric.
```

```
    We detect those zero-crossings of psi(t) mod pi, then sample the phase
    of V at those instants.

    Returns:
      t_strobes      - times of neutral crossings
      theta_strobes  - phase(V) mod 2*pi at those crossings
    """
    psi        = phi_V - phi_M
    psi_unwrap = np.unwrap(psi)

    # Fold modulo pi into (-pi/2, +pi/2] to catch both +/- cross
    psi_fold = ((psi_unwrap + 0.5*np.pi) % np.pi) - 0.5*np.pi

    t_strobes     = []
    theta_strobes = []

    for i in range(len(t)-1):
        # crossing from negative to positive
        if (psi_fold[i] < 0.0) and (psi_fold[i+1] >= 0.0):
            frac = (-psi_fold[i]) / (psi_fold[i+1] - psi_fold[i] + 1e-15)
            t_cross = t[i] + frac*(t[i+1] - t[i])

            # interpolate V-phase at crossing
            phiV_cross = phi_V[i] + frac*(phi_V[i+1] - phi_V[i])
            theta = np.mod(phiV_cross, 2.0*np.pi)

            t_strobes.append(t_cross)
            theta_strobes.append(theta)

    return np.array(t_strobes), np.array(theta_strobes)

def fit_even_map(theta):
    """
    Build the neutral stroboscopic map:

      theta_n   = phase(V) at the nth neutral crossing
      Delta_theta_n = theta_{n+1} - theta_n

    Model:
      Delta_theta_n = Omega - K2 * sin(2 * theta_n)

    We fit [Omega, K2] by linear regression of
      Delta_theta_n  vs  [1, sin(2*theta_n)].

    Returns:
      Omega_hat, K2_hat,
      stderr_Omega, stderr_K2,
      (theta_n, dtheta, dtheta_fit)
```

```
    """
    if len(theta) < 3:
        return (np.nan, np.nan,
                np.nan, np.nan,
                (np.array([]), np.array([]), np.array([])))

    th0    = theta[:-1]
    th1    = theta[1:]
    dtheta = th1 - th0

    # wrap dtheta into (-pi, pi]
    dtheta = ((dtheta + np.pi) % (2.0*np.pi)) - np.pi

    # Regression design matrix for:
    #   dtheta = a + b * sin(2*theta)
    X = np.column_stack((np.ones_like(th0), np.sin(2.0*th0)))
    y = dtheta

    beta, _, _, _ = lstsq(X, y, rcond=None)
    a, b = beta[0], beta[1]   # a ~ Omega_hat, b ~ (-K2_hat)

    # Estimate standard errors assuming iid residuals
    if len(y) > 2:
        dof    = len(y) - 2
        sigma2 = np.sum((y - X @ beta)**2) / (dof if dof > 0 else 1)
    else:
        sigma2 = np.sum((y - X @ beta)**2)

    XtX_inv   = np.linalg.inv(X.T @ X)
    cov_beta  = sigma2 * XtX_inv
    stderr_a  = np.sqrt(cov_beta[0,0])
    stderr_b  = np.sqrt(cov_beta[1,1])

    Omega_hat = a
    K2_hat    = -b            # minus sign by convention
    stderr_Om = stderr_a
    stderr_K2 = stderr_b

    dtheta_fit = X @ beta     # fitted Delta_theta_n

    return Omega_hat, K2_hat, stderr_Om, stderr_K2, (th0, dtheta, dtheta_fit)

# ------------------------
# 4. Run pipeline and plot the final multi-panel figure
# ------------------------

# Generate synthetic simultaneous V(t), M(t)
t, Vsig, Msig, fs = generate_synthetic_dual_channel()
```

```
# Power spectra
fV, PV = welch_psd(Vsig, fs)
fM, PM = welch_psd(Msig, fs)

# Identify fast carrier peaks and beat frequency
FAST_BAND = (0.5, 2.0)  # Hz range where we expect the ~1 Hz carriers
f_plus, f_minus, f_slow = find_two_carriers(fV, PV, FAST_BAND)

# Coherence spectrum and its slow-band value
fCoh, Coh = coherence_spectrum(Vsig, Msig, fs)
Lambda_fslow = get_coherence_at_frequency(fCoh, Coh, f_slow, rel_window=0.15)

# Neutral stroboscopic map
phi_V = unwrap_phase(Vsig)
phi_M = unwrap_phase(Msig)
t_strobe, theta_strobe = neutral_strobe(t, phi_V, phi_M)

Omega_hat, K2_hat, se_Om, se_K2, mapdata = fit_even_map(theta_strobe)
th0, dtheta, dtheta_fit = mapdata

# Predicted lock 2/21:
Omega_lock_2_21 = np.pi * (2.0/21.0)
lock_dist       = np.abs(Omega_hat - Omega_lock_2_21)

# ------------------------
# 5. Create the final figure with a stats header on top
# ------------------------

outdir = "figs"
os.makedirs(outdir, exist_ok=True)

fig, axes = plt.subplots(
    5, 1,
    figsize=(7, 12),
    gridspec_kw={"height_ratios":[0.8, 1.8, 1.8, 1.8, 2.2],
                 "hspace": 0.6}
)

ax_stats, ax_ts, ax_psd, ax_coh, ax_map = axes

# Panel 0: stats header (text only, ASCII-safe)
ax_stats.axis("off")

header_text = (
    "fs = %.1f Hz | "
    "f_plus = %.3f Hz | "
    "f_minus = %.3f Hz | "
```

```
    "f_slow = %.3f Hz | "
    "Lambda(f_slow) = %.3f\n"
    "Omega_hat = %.3f +/- %.3f rad | "
    "K2_hat = %.3f +/- %.3f\n"
    "Omega_2over21 = pi*2/21 ~= %.3f rad | "
    "|Omega_hat - Omega_2over21| = %.3f rad"
    % (fs,
       f_plus, f_minus, f_slow, Lambda_fslow,
       Omega_hat, se_Om, K2_hat, se_K2,
       Omega_lock_2_21, lock_dist)
)

ax_stats.text(
    0.01, 0.5, header_text,
    ha="left", va="center", fontsize=8,
    bbox=dict(facecolor="white", edgecolor="gray", alpha=0.9)
)

# Panel 1: simultaneous traces V(t) and M(t)
ax_ts.plot(t, Vsig, label="V(t) (voltage-like)", linewidth=0.8)
ax_ts.plot(t, Msig, label="M(t) (mechanical-like)", linewidth=0.8, alpha=0.8)
ax_ts.set_title("Simultaneous electromechanical traces (synthetic)")
ax_ts.set_xlabel("time (s)")
ax_ts.set_ylabel("z-scored signal")
ax_ts.legend(loc="upper right", fontsize=8)

# Panel 2: power spectra with peaks
ax_psd.semilogy(fV, PV, label="PSD[V]", linewidth=0.8)
ax_psd.semilogy(fM, PM, label="PSD[M]", linewidth=0.8, alpha=0.8)
if not np.isnan(f_plus):
    ax_psd.axvline(f_plus, ls="--", color="tab:orange",
                   label="f_plus ~ %.2f Hz" % f_plus)
if not np.isnan(f_minus):
    ax_psd.axvline(f_minus, ls="--", color="tab:green",
                   label="f_minus ~ %.2f Hz" % f_minus)

ax_psd.set_title("Power spectra of V and M (synthetic dual-channel)")
ax_psd.set_xlabel("frequency (Hz)")
ax_psd.set_ylabel("power")
ax_psd.legend(fontsize=8)

# Panel 3: coherence Lambda(f) and slow-band marker
ax_coh.plot(fCoh, Coh, linewidth=0.8, color="tab:blue")
if not np.isnan(f_slow):
    ax_coh.axvline(
        f_slow,
        ls="--",
        color="red",
```

```
        label=("f_slow ~ %.2f Hz, Lambda ~ %.2f" %
               (f_slow, Lambda_fslow))
    )
ax_coh.set_ylim(0, 1.05)
ax_coh.set_title("Electromechanical coherence (synthetic)")
ax_coh.set_xlabel("frequency (Hz)")
ax_coh.set_ylabel("Lambda(f)")
ax_coh.legend(loc="upper right", fontsize=8)

# Panel 4: neutral stroboscopic map and even-harmonic fit
ax_map.scatter(th0, dtheta, s=12, alpha=0.6,
               label="data", color="tab:blue")
if len(th0) > 0:
    order = np.argsort(th0)
    ax_map.plot(th0[order], dtheta_fit[order],
                color="red", linewidth=1.5,
                label="fit: Delta_theta = Omega - K2*sin(2*theta)")

# Small textbox summarizing Omega_hat etc. (ASCII-safe)
box_text = (
    "Omega_hat ~= %.3f rad, K2_hat ~= %.3f\n"
    "Omega_2over21 ~= %.3f rad\n"
    "|Omega_hat - Omega_2over21| ~= %.3f rad"
    % (Omega_hat, K2_hat, Omega_lock_2_21, lock_dist)
)
ax_map.text(
    0.02, 0.98, box_text,
    ha="left", va="top",
    transform=ax_map.transAxes,
    fontsize=8,
    bbox=dict(facecolor="white", edgecolor="gray", alpha=0.9)
)

ax_map.set_title("Neutral stroboscopic map (synthetic)")
ax_map.set_xlabel("theta_n (phase of V at neutral strobe)")
ax_map.set_ylabel("theta_{n+1} - theta_n")
ax_map.legend(loc="lower left", fontsize=8)

plt.tight_layout()
outpath = os.path.join(outdir, "Level1_full.png")
plt.savefig(outpath, dpi=300)
plt.show()
print("Saved figure to", outpath)
```

25 Glossary of symbols

This appendix summarizes the main symbols used in the slow-phase locking analysis, the coherence readout Λ, and the phase-targeted entrainment protocol. Unless noted otherwise, quantities are evaluated under neutral-moment strobing (even parity) and at

the mesoscale wavenumber $k^* = \pi/\ell$.

Symbol	Units	Meaning / operational definition
ℓ	m	Effective cortical (shell) thickness setting the mesoscale.
k^*	m^{-1}	Mesoscale wavenumber where carriers are evaluated: $k^* = \pi/\ell$.
D_V	m^2/s	Effective voltage diffusivity / gap-junctional spread parameter.
τ_m	s	Membrane (RC) charging time.
ρ_{eff}	kg/m^2	Effective areal inertia of the cortical layer.
κ	N/m	Effective cortical stiffness / tension modulus.
η	N·s/m	Effective cortical viscosity (loss).
D_σ	m^2/s	Effective stress diffusion / mechanical spreading.
β_R, β_I	V/Pa (or eq.)	In-phase (β_R) and quadrature (β_I) components of mechanical $\rightarrow$ electrical coupling.
γ	m/V (or Pa/V)	Electrical $\rightarrow$ mechanical coupling gain (voltage drive on cortical stress / displacement).
ϕ_c	rad	Electromechanical coupling phase, $\phi_c = \arg(\beta_R + i\beta_I)$, which sets the lag between electrical drive and mechanical response.
$C_{V\sigma}(f)$	–	Magnitude-squared coherence between V and σ at frequency f.
$S_V(f), S_\sigma(f)$	arb.	Power spectral densities (Welch) of V and σ.
$S_V^{\mathrm{slow}}(f), S_\sigma^{\mathrm{slow}}(f)$	arb.	Slow-band spectra: band-passed power near f_{slow}.
$\omega_{\pm,r}$	rad/s	Real parts of the carrier angular frequencies at k^*; $\omega_{\pm,r} = 2\pi f_\pm$.

Table 4: Material / biophysical parameters and readouts: mechanical and electrical couplings, spectra, and coherence.

Symbol	Units	Meaning / operational definition
f_{drive}	Hz	Driving frequency applied during phase-targeted entrainment. Chosen to match the measured f_{slow} (on-band) for that specific culture / dish.
f_{ctrl}	Hz	Off-resonant control frequency, typically $f_{\mathrm{ctrl}} = f_{\mathrm{slow}} \cdot (1+0.10)$ ($\sim 10\%$ higher than f_{slow}), with the same amplitude and duty cycle. Used to test frequency specificity.
$\Delta\Lambda$	–	Change in slow-band coherence during stimulation, $\Delta\Lambda = \Lambda_{\mathrm{in}} - \Lambda_{\mathrm{out}}$, where $\Lambda_{\mathrm{in}} \equiv C_{V\sigma}(f_{\mathrm{slow}})$ inside the driven window and Λ_{out} is baseline / undriven. Positive $\Delta\Lambda$ indicates improved locking at f_{slow}.
ρ	–	Winding number (slow-phase advance per strobe) in the original 2π convention; used in the "devil's staircase" view of locking. By contrast, ρ_π is defined in the mod π (even-parity) convention.
π	rad	Angular constant ($\pi \simeq 3.1416$) used to define locking ratios and map conventions, e.g. $\Omega = \pi \cdot 2/21$.

Table 5: Entrainment and control variables: drive frequencies, coherence gain, and winding numbers.

Symbol	Units	Meaning / operational definition
$V(\mathbf{x}, t)$	V (arb.)	Bioelectric field / membrane potential readout (optical electrophysiology).
$\sigma(\mathbf{x}, t)$	Pa (stress)	Cortical / tensional stress field inferred from traction force microscopy, AFM, etc.
$u(\mathbf{x}, t)$	m	Latent in-plane cortical displacement from which σ is defined.
f_-, f_+	Hz	Carrier frequencies of the two weakly coupled underdamped electromechanical modes (electrical-leaning and mechanical-leaning branches). Typically in the 1–3 Hz band.
f_{slow}	Hz	Slow interference cadence, $f_{\text{slow}} = \lvert f_+ - f_- \rvert$; appears as a shared slow-band peak in V and σ.
r_{eff}	–	Carrier ratio $r_{\text{eff}} = f_-/f_+$, used to estimate the slow forcing Ω.
Ω	rad	Effective slow-phase forcing in the even (mod π) map, estimated from neutral-moment stroboscopy. Operationally $\Omega \simeq \frac{\pi}{2}(1 - r_{\text{eff}})$.
K_2	rad	Even-harmonic coupling strength in the slow-phase map, obtained by regressing $\Delta\theta_n$ onto $\sin(2\theta_n)$ at neutral moments.
θ_n	rad	Slow phase of the fast "+" carrier, sampled stroboscopically at successive neutral moments ($\theta \sim \theta + \pi$ in the even convention).
$\Delta\theta_n$	rad	One-step slow-phase increment, $\Delta\theta_n = \theta_{n+1} - \theta_n$ (unwrapped).
Λ	–	Slow-band electromechanical coherence, $\Lambda \equiv C_{V\sigma}(f_{\text{slow}})$, i.e. magnitude-squared coherence between V and σ at f_{slow}. $\Lambda \in [0, 1]$.
ρ_π	–	Locked winding number of the slow phase in the even (mod π) convention: ratio between slow-phase advance and the neutral-moment strobe. Physiologically relevant plateau: $\rho_\pi = 2/21$.

Table 6: Dynamical / locking variables: slow cadence, slow-phase map, and coherence.

Acknowledgments

This manuscript was prepared with the assistance of AI-based editing and drafting tools. The author retains full responsibility for the analysis, interpretation, and any errors.

References

[1] S. H. Strogatz, *Nonlinear Dynamics and Chaos*, Westview (2018).

[2] A. Pikovsky, M. Rosenblum, J. Kurths, *Synchronization: A Universal Concept in Nonlinear Sciences*, Cambridge (2001).

[3] J. Keener, J. Sneyd, *Mathematical Physiology*, Springer (2009).

[4] M. Levin, Bioelectric signaling: Reprogrammable circuits governing growth and form, *Cell* **184** (2021) 197–205.

[5] B. Machta et al., Mechanics and active fluctuations of the cell cortex, *Annu. Rev. Condens. Matter Phys.* (2019).

[6] S. Denisov, Synchronization and the circle map, *Physics Reports* (review).

[7] V. I. Arnold, Small denominators and problems of stability of motion in classical and celestial mechanics, *Russian Mathematical Surveys* **18** (1963) 85–191.

[8] L. Cohen, *Time–Frequency Analysis*, Prentice Hall (1995).

[9] G. Shim, I. B. Breinyn, A. Martínez-Calvo, S. Rao, and D. J. Cohen, Bioelectric stimulation controls tissue shape and size, *Nature Communications* **15**, 2938 (2024). doi:10.1038/s41467-024-47079-w.

[10] J. Cervera, M. Levin, and S. Mafé, Multicellular adaptation to electrophysiological perturbations analyzed by deterministic and stochastic bioelectrical models, *Scientific Reports* **14**, 27608 (2024). doi:10.1038/s41598-024-79087-7.